iScience

CellPress
OPEN ACCESS

Article

Mitoribosome Defect in Hepatocellular Carcinoma Promotes an Aggressive Phenotype with Suppressed Immune Reaction

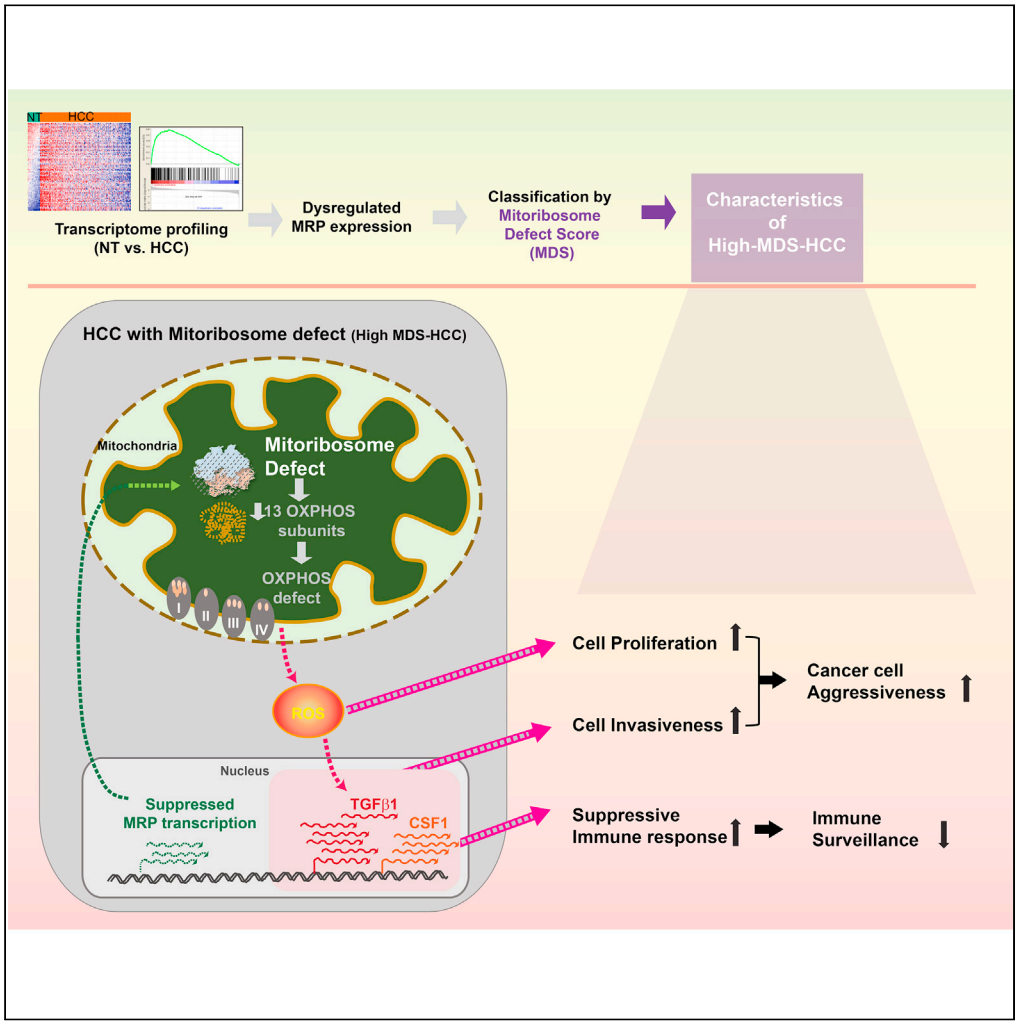

So Mee Kwon, Young-Kyoung Lee, Seongki Min, Hyun Goo Woo, Hee Jung Wang, Gyesoon Yoon

smkwon@ajou.ac.kr (S.M.K.)
ypeace@ajou.ac.kr (G.Y.)

HIGHLIGHTS

A set of down-regulated MRPs in HCC cause mitoribosomal defects

Mitoribosomal defects are linked to aggressive molecular features and poor prognosis

Mitoribosomal defects in HCC are associated with immunosuppression and evasion

TGF-β signaling pathway is a crucial mechanism to mediate mitoribosomal defects in HCC

Kwon et al., iScience 23, 101247
June 26, 2020
https://doi.org/10.1016/j.isci.2020.101247

iScience

CellPress
OPEN ACCESS

Article

Mitoribosome Defect in Hepatocellular Carcinoma Promotes an Aggressive Phenotype with Suppressed Immune Reaction

So Mee Kwon,[1,2,3,5,*] Young-Kyoung Lee,[2,3] Seongki Min,[2,3] Hyun Goo Woo,[1,3] Hee Jung Wang,[4] and Gyesoon Yoon[2,3,*]

SUMMARY

Mitochondrial ribosomes (mitoribosomes), the specialized translational machinery for mitochondrial genes, exclusively encode the subunits of the oxidative phosphorylation (OXPHOS) system. Although OXPHOS dysfunctions are associated with hepatic disorders including hepatocellular carcinoma (HCC), their underlying mechanisms remain poorly elucidated. In this study, we aimed to investigate the effects of mitoribosome defects on OXPHOS and HCC progression. By generating a gene signature from HCC transcriptome data, we developed a scoring system, i.e., mitoribosome defect score (MDS), which represents the degree of mitoribosomal defects in cancers. The MDS showed close associations with the clinical outcomes of patients with HCC and with gene functions such as oxidative phosphorylation, cell-cycle activation, and epithelial-mesenchymal transition. By analyzing immune profiles, we observed that mitoribosomal defects are also associated with immunosuppression and evasion. Taken together, our results provide new insights into the roles of mitoribosome defects in HCC progression.

INTRODUCTION

Mitochondria are key organelles with pivotal roles in the bioenergetic and biosynthetic processes of cells. The main function of mitochondria, which are often regarded as the powerhouse of cells, is ATP production through oxidative phosphorylation (OXPHOS). Mitochondrial OXPHOS plays a central role in energy production, which is vital to maintain cellular function and physiology (Zong et al., 2016). There is accumulating evidence for impaired OXPHOS activity in many solid tumor cells (Chandra and Singh, 2011). Furthermore, OXPHOS defects have been described as one of the most common and prominent phenotypes of most cancers (Chandra and Singh, 2011; Warburg, 1956) and are often implicated in several cancer hallmarks (Hanahan and Weinberg, 2011), such as genomic instability (Martinez-Outschoorn et al., 2010), tumor-promoting inflammation (Sukumar et al., 2017; Colegio et al., 2014), and metastasis (LeBleu et al., 2014; Nunes et al., 2015). Mitochondria possess their own mitochondrial DNA (mtDNA) genome and the corresponding replication, transcription, and translation machinery required for its maintenance and expression. Human mtDNA encodes 13 hydrophobic core subunits of the OXPHOS system, as well as 2 rRNAs and 22 tRNAs. These 13 proteins are synthesized in the specialized translation machinery called *mitochondrial ribosome*, also known as the mitoribosome (De Silva et al., 2015). Mitoribosome is a macrostructure of dual genetic origin, formed by two mitoribosomal RNA components encoded by mtDNA and 82 mitoribosomal proteins (MRPs) encoded by nuclear DNA. Therefore, the balanced expression of rRNAs and MRPs and their well-coordinated assembly are essential for regulation of OXPHOS activity and the resultant energy production.

Recent advances in genomics and proteomics have provided information on the contribution of mitoribosome composition and function in the initiation and promotion of tumors. Many studies have shown that altered expression of several MRPs is closely associated with cancer development and progression as well as the metastasis of many cancer types (Loo et al., 2012; Pu et al., 2017; Sorensen et al., 2017; Wei et al., 2019). For example, *MRPL11* was decreased in the primary tumor tissues of head and neck squamous cell carcinoma (HNSCC) and was considered a potential biomarker for HNSCC (Koc et al., 2015). In addition, the alternative role of several MRPs, such as *DAP3* (Levy-Strumpf and Kimchi, 1998), *MRPS30/PDCD9* (Carim et al., 1999), and *MRPL41* (Chintharlapalli et al., 2005), as apoptosis-inducing factors has been

[1]Departments of Physiology, Ajou University School of Medicine, Suwon 16499, Korea

[2]Departments of Biochemistry, Ajou University School of Medicine, Suwon 16499, Korea

[3]Departments of Biomedical Sciences, Ajou University School of Medicine, Suwon 16499, Korea

[4]Departments of Surgery, Ajou University School of Medicine, Suwon 16499, Korea

[5]Lead Contact

*Correspondence: smkwon@ajou.ac.kr (S.M.K.), ypeace@ajou.ac.kr (G.Y.)

https://doi.org/10.1016/j.isci.2020.101247

reported. However, the mechanisms underlying the contribution of MRP alterations to cancer progression remain poorly understood. Moreover, these studies have a limitation on substantiating how MRP alterations affect mitochondrial functions systematically.

As a central organ in a variety of critical biological functions such as homeostasis of carbohydrate, lipid, amino acid, and protein synthesis, the liver is heavily enriched with mitochondria in terms of number and density (Degli Esposti et al., 2012), compared with other organs. In addition, most liver diseases including alcoholic liver disease, non-alcoholic fatty liver disease, non-alcoholic steatohepatitis, viral hepatitis, and HCC are characterized by mitochondrial dysfunction and are associated with accumulation of damaged mitochondria (Auger et al., 2015). Therefore, MRP alteration might play critical roles in the pathophysiology of liver diseases such as HCC. We have previously reported that reduced expression of MRPL13 is a cause of OXPHOS defects in HCC and promotes the invasiveness of OXPHOS-defective HCC cells, suggesting the potential involvement of mitoribosomal defects in liver cancer progression (Lee et al., 2017). However, it is unclear whether MRPL13 depletion is the only cause for cancerous OXPHOS defects and the associated aggressive phenotype of HCC.

In this study, we demonstrated that patients with HCC with mitoribosome defects had poor prognostic outcomes. In addition, we observed that HCCs with mitoribosome defects exhibited suppressive immune responses, which may allow tumor cells to evade immune surveillance and develop.

RESULT

Mitoribosomal Defect Gene Signature Is a Good Indicator of HCC Prognosis

To elucidate whether mitoribosomal defects are the only primary cause for the OXPHOS defects seen in HCC, we compared mitochondrial biogenesis by investigating mitochondrial translation, transcription, and replication between paired tumors (T) and surrounding tissues (ST) obtained from 15 patients with HCC (Table S1). Among 15 tumor tissues, 8 tissues (53%) showed lower protein levels of COX2, which is an important mtDNA-encoded core subunit of the OXPHOS complex IV, compared with their paired surrounding tissues (Figures S1A–S1E). Unexpectedly, among those 8 tissues, only one case showed decreased protein levels of mitochondrial transcription factor A (TFAM), a key mitochondrial transcription factor. However, the other cases harbored even higher TFAM levels (Figures S1A and S1C). Moreover, when we further examined the mtDNA copy number, only one case of eight tumor tissues showed a slight decrease in mtDNA levels (Figures S1A and S1D). These results imply that mitochondrial replication and its transcription activity are not the main contributors to the low expression of an mtDNA-encoded protein (Figure S1E).

As the mitoribosome, comprising 82 MRPs (Pietromonaco et al., 1991), is a huge and complex structure, it is plausible that co-expression of MRPs may play a critical role in the mitoribosome assembly and translation into functional proteins. With this concern, we examined the expression of MRPs in HCC by analyzing The Cancer Genome Atlas (TCGA) transcriptome data (n = 371, Figure 1A). Interestingly, we observed that the distribution of overall expression levels of MRPs was not different between non-tumor (NT) and primary tumor (PT) tissues (Figure 1B). However, the NT group showed a well-coordinated expression of MRPs in each sample, whereas the PT group showed more diverse expression levels of MRPs in each sample (Figures 1C and 1D). Moreover, the NT group, compared with the PT group, showed a closer correlation among the expression levels of MRPs (Figures S2A and S2B). These results imply that the NT group had intact mitoribosomal integrity, showing a well-coordinated expression of MRPs, whereas the PT group lost its mitoribosomal integrity and showed dysregulated expression of MRPs. Thus, we suggest that the dysregulated MRP expression in HCC may play important roles in HCC development or progression.

To evaluate whether the expression of MRPs contributes to the development and progression of HCC, we generated three unique MRP signatures, 12 up-MRPs, 6 down-MRPs, and 20 other-MRPs, by comparing the MRP expression between PT and NT (permuted Student's t test $p < 0.05$ and fold difference >0.3, Transparent Methods; Figures 1A and 1E; Table S2). Thereafter, by performing gene set enrichment analysis (GSEA), the expression enrichment of these signatures was measured in each of the tumor samples (Figure 1E). Interestingly, most HCC samples demonstrated higher expression of up-MRPs and lower expression of the down-MRPs. This may indicate that the expression of each of the up-MRPs and down-MRPs is well coordinated in tumor cells.

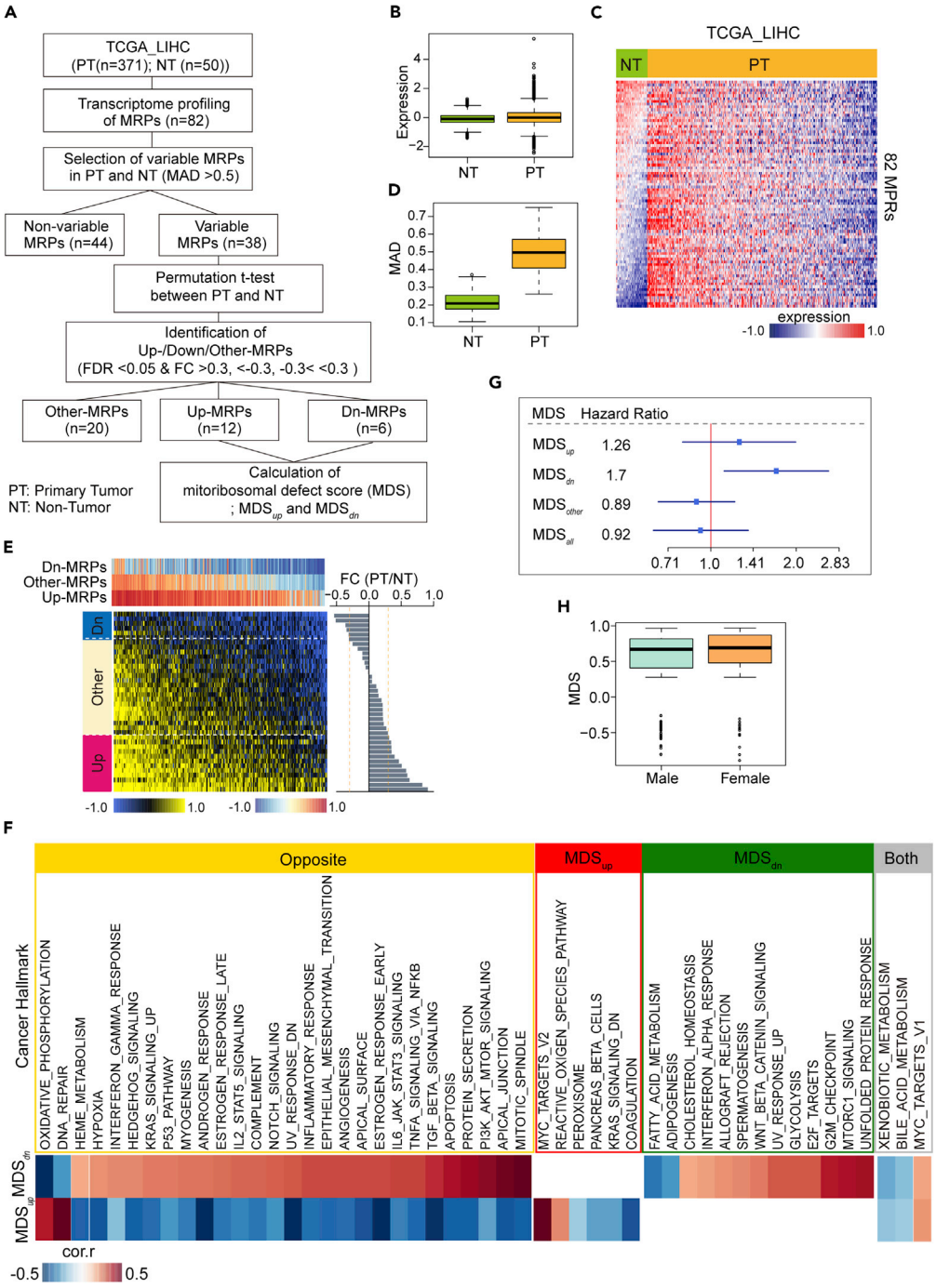

Figure 1. Mitoribosomal Defect Gene Signature Is a Good Indicator of HCC Prognosis

(A) Schematic view of the analysis of MRPs to define three distinctive signatures (Up-MRPs, Dn-MRPs, and Other-MRPs).

(B) Comparison of MRPs' expression between NT and PT.

(C) Heatmap shows the expression of 82 MRPs in 371 PT and 50 NT samples from TCGA-LIHC cohort.

(D) Comparison of maximum absolute deviation (MAD) among MRPs' expression between NT and PT.

(E) (Top) Enrichment of three distinctive signatures (Up-MRPs, Dn-MRPs, and Other-MRPs) among PT. (Bottom) Heatmap shows the expression of variable MRPs (n = 38) among PT. (Right) Bar plot indicates the fold difference in the expression of variable MRPs (n = 38) between PT and NT.

(F and G) Mitoribosome defect scores (MDSs) were calculated based on the three distinctive signatures (Up-MRPs, Dn-MRPs, and Other-MRPs) and total MRPs; MDS_{up}, MDS_{dn}, MDS_{other}, and MDS_{all}, respectively. Heatmap indicates the

Figure 1. *Continued*

association of MDS_{up} and MDS_{dn} with Cancer Hallmark gene sets. According to the direction of the association between MDS_{up} and MDS_{dn}, gene sets were classified into the opposite, Only-MDS_{up}, Only-MDS_{dn}, or common, which were associated with MDS_{up} and MDS_{dn} in the opposite manner, MDS_{up} specifically, MDS_{dn} specifically, or in the same direction, respectively. A positive or negative association is shown in red or blue, respectively. Gene set with a non-significant association ($p > 0.001$) is shown in the blank (F). Forest plot indicates hazard ratios for MDSs based on the Cox-regressional univariate survival analysis (G).

(H) Comparison of MDS between male (n = 250) and female (n = 121) samples from TCGA-LIHC cohort. Boxplots of MDSs of males and females are shown as first quartile, median, and third quartile (bottom box, middle line, and top box, respectively). Whiskers represent the minimum and maximum values.

See also Figures S1 and S2; Table S2 and Table S3

To estimate the degree of mitoribosome defects in individual samples, we then designated the enrichment scores (NES, normalized enrichment score) of the three MRP signatures (up-MRPs, down-MRPs, or other-MRPs) and transformed the NES as mitoribosome defects scores (MDS), MDS_{up}, MDS_{dn}, and MDS_{other}, to reflect the direction of the up and down signatures (see Transparent Methods). When evaluating whether these MDSs were associated with cancer-related features using 50 cancer hallmark gene sets (Liberzon et al., 2015) (see Transparent Methods), we observed that most of the cancer gene sets showed closely correlated expressions with MDS_{dn} and negatively correlated expression with MDS_{up} (Figure 1F; Table S3). In addition, MDS_{dn} showed significant correlations with the expression of gene sets for the unfolded protein response ($r = 0.417$, $p = 5.083 \times 10^{-17}$) and glycolysis ($r = 0.308$, $p = 1.303 \times 10^{-9}$) and negative correlations with lipid metabolism-related gene sets (i.e., fatty acid metabolism and adipogenesis) (Figure 1F; Table S3). Remarkably, MDS_{dn} showed the strongest negative correlation with OXPHOS ($r = -0.565$, $p = 1.020 \times 10^{-32}$). This may imply that mitoribosomal defects induced by the suppression of down-MRPs are closely associated with OXPHOS dysfunction. Moreover, survival analysis based on the Cox regressional hazard model showed that only MDS_{dn} was significantly associated with poor prognosis ($p = 8.479 \times 10^{-3}$) (Figure 1G). These results suggest that mitoribosomal defects invoked by the decreased expression of down-MRPs may play a critical role in HCC prognosis. In addition, these findings indicate that MDS_{dn} is a good indicator of mitochondrial dysfunction and HCC prognosis, emphasizing that our MDS scoring system is an important new tool that successfully reflects the mitochondrial dysfunction-related cancer features in HCC. Furthermore, there was no significant difference found in the comparison of MDS between males (n = 250) and females (n = 121), implying that mitoribosomal defects may not be affected by sex differences (Figure 1H).

Identification of Molecular Features Linked to Mitoribosomal Defects

To advance the clarification of the underlying molecular features related to mitoribosomal defects in HCC, we stratified TCGA HCC samples into high- and low-mitoribosome defect (MD) subtypes, i.e., H-MD (>upper quartile MDS_{dn}) and L-MD (<lower quartile MDS_{dn}), respectively. GSEA analysis (MsigDB. V. 6.1) revealed that H-MD was depleted in the mitochondrial function-related gene sets, such as OXPHOS, fatty acid metabolism, and reactive oxygen species (ROS) pathway, as well as the mitochondrial structure-related gene sets, such as mitochondrial matrix, envelope, membrane, and protein complex (Table S4; Figures 2A, 2B, and S3A–S3C). In contrast, the H-MD group revealed enriched expression of cell cycle-related gene sets (i.e., mitotic spindle, PI3K/AKT/mTOR axis signaling). Other cancer-related gene sets were also enriched in the H-MD, including transforming growth factor (TGF)-β signaling (Caja et al., 2018), WNT/β-catenin signaling (Khalaf et al., 2018), nuclear factor-κB signaling (Luedde and Schwabe, 2011), epithelial to mesenchymal transition (EMT), inflammatory response, and interleukin (IL)-6/JAK/STAT3 axis signaling (Table S4; Figures 2C and S4A–S4C). These results indicate that mitochondrial dysfunction, as a result of mitoribosomal defects, may be critically involved in cell transformation and progression of aggressive HCC. Furthermore, in the Kaplan-Meier survival analysis, the H-MD group showed worse prognostic outcomes of overall survival compared with L-MD (Figure 2D). By comparing the gene expression between H-MD and L-MD, we identified 83 upregulated and 161 downregulated differentially expressed genes (DEGs) in H-MD (permutated Student's t test false discovery rate [FDR] <0.005 and fold change >1, Figures 2E–2G; Table S5). Among the upregulated DEGs, immune response-related genes, such as secreted phosphoprotein 1 (*SPP1*), integrin subunit beta 1 (*ITGB1*), and immunoglobulin heavy constant gamma 1 (*IGHG1*), as well as cell adhesion-related genes such as *CD24*, stratifin (*SFN*), and epithelial cell adhesion molecule (*EPCAM*), were the most highly expressed in H-MD (Figure 2E, *pink-colored box*). On the contrary, genes related to metabolism, such as carbamoyl-phosphate synthase 1 (*CPS1*), serum amyloid A1 (*SAA1*), cytochrome P450 family 8 subfamily B member 1 (*CYP8B1*), and tyrosine aminotransferase (*TAT*),

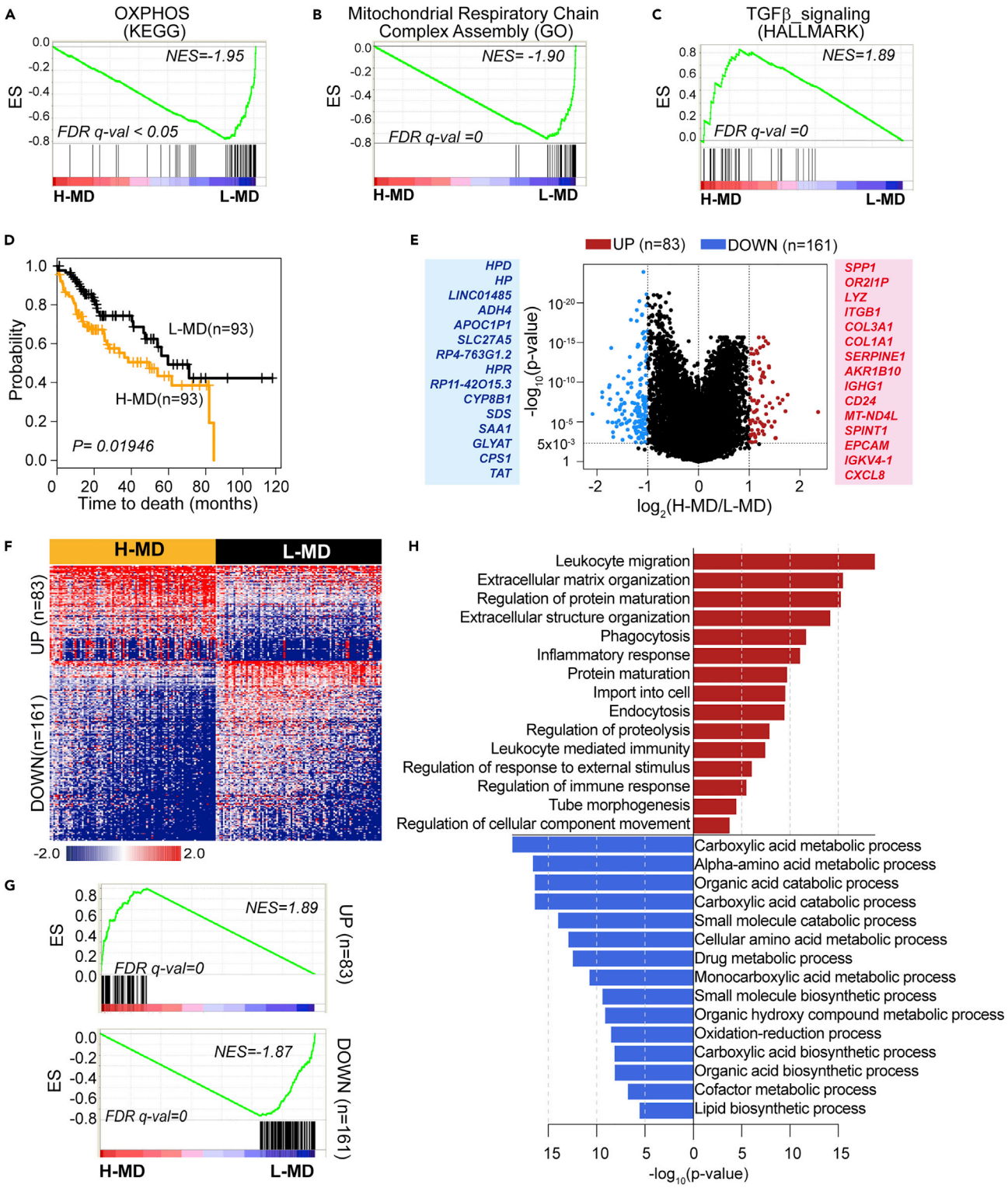

Figure 2. Identification of Molecular Features Linked to Mitochondrial Defects

Based on the MDS_{dn}, TCGA-LIHC samples were stratified into the subgroup with higher mitoribosome defect (H-MD) and one with lower mitoribosome defect (L-MD), and molecular features associated with H-MD or L-MD were compared.

(A–C) GSEA results based on the OXPHOS (A), mitochondria respiratory chain complex assembly (B), and TGF-β signaling (C) were shown. Normalized enrichment scores (NES) and FDR for each gene set are noted.

Figure 2. *Continued*

(D) Overall survival time of H-MD and L-MD was compared based on the Kaplan-Meier survival analysis.

(E) Volcano plot indicates fold change (FC) and FDR based on the permutation t test between H-MD and L-MD groups. Differentially expressed genes (DEGs) were marked with red- or blue-colored points (FC > 1 or < −1 & FDR <0.005, respectively).

(F) The expression of upregulated (n = 83) or downregulated (n = 161) DEGs in either H-MD or L-MD is shown. Samples are represented in columns, grouped by H-MD or L-MD.

(G) Enrichment plots based on the 83 upregulated genes and 161 downregulated genes are shown in the left and right panels, respectively. NES and FDR for each gene set are noted.

(H) Gene ontology (GO) analysis was performed based on the up and down DEGs. The -$\log_{10}$(p value) is shown in red and blue bars for up- and downregulated genes, respectively.

See also Figure S3; Table S4 and S5.

showed the lowest expression in the H-MD group (Figure 2E, *blue-colored box*). Interestingly, according to the Human Protein Atlas (Uhlen et al., 2015) (https://www.proteinatlas.org/), more than half of the downregulated DEGs (82/161) are liver tissue-specific genes, including *CPS1*, *SAA1*, *TAT*, and *HPD*, indicating that mitoribosomal integrity is also essential in maintaining the liver's intrinsic functions (Table S5). Similarly, Gene Ontology (GO) analysis of DEGs demonstrated that genes involved in fundamental mitochondrial functions such as catabolic, biosynthetic process and oxidation-reduction processes were significantly downregulated, whereas those linked to immune cell infiltration, inflammatory response, and extracellular matrix (ECM) organization were highly upregulated in H-MD (Figure 2H). These results indicate the potential impact of mitoribosome defects on the tumor microenvironment concerning the immune response.

Mitoribosomal Defects Are Closely Associated with Immune Cell Response in HCC

Based on GO analysis, we interrogated the relevance of mitoribosomal defects to immune response signaling in detail. First, we employed the recently reported immune signatures (n = 112) derived from an immune-specific subclass of HCC (Sia et al., 2017). The H-MD group showed higher enrichment for the overall HCC immune signature (Sia et al., 2017) than did the L-MD group (Figure 3A). Furthermore, among the immune system genes with significantly higher expression in H-MD (n = 21, permutated Student's t test FDR <0.01 and fold change >0.5; Figure S4A), *COL1A1*, *COL1A2*, and *POSTN* were prominently expressed in the H-MD group (Figure S4A). Considering their function in ECM, we investigated whether or not mitoribosomal defects were associated with cancer-associated ECM (C-ECM). It was observed that the H-MD group was enriched with the C-ECM signature (Chakravarthy et al., 2018) (Figure 3B). Furthermore, the H-MD group was enriched with the activated stroma-related genes (Moffitt et al., 2015), but not with normal stroma-related genes (Moffitt et al., 2015) (Figures 3C and 3D). These results are indicative of the possibility that mitoribosome defects may selectively affect the neighboring cells to perturb the HCC microenvironment. To delineate the repertoire of neighboring cells in the microenvironment, we used the inferred proportion for 64 immune and stromal cell types based on *xCell* analysis (Aran et al., 2017) and compared the proportion of infiltrated immune cells between H-MD and L-MD (see Transparent Methods, and Figures 3E and 3F; Table S5). Interestingly, suppressive immune cells favorable for cancer cells including mast cells, Th2 cells, and regulatory T cells showed more infiltration (Figure 3E), whereas stimulatory immune cells related to anti-cancer immunity such as CD8+ naive T cells, NK T cells (NKT), and Th1 cells were less infiltrated in the H-MD than in the L-MD subtype (Figure 3F). These results suggest that mitoribosome defects may contribute to the creation of a more favorable microenvironment by suppressing immune responses and promoting evasion from immune surveillance. Next, we examined the link of mitoribosomal defects with immune-modulatory cytokines using 25 immune inhibitors, 28 immune stimulators, 6 major histocompatibility complex (MHC) class I, 10 MHC class II, and 3 MHC non-classified molecules (Transparent Methods, Table S7). This analysis revealed that most cytokines, except for *IL6R* and *ICOSLG* (*green-colored box*), were more highly expressed in the H-MD than in the L-MD subtype and were positively associated with mitoribosomal defects (Figure 3G), implying a more active immune contexture of the H-MD group.

Among the immune molecules, *TGFB1* was the most highly expressed gene in H-MD with a significant association with mitoribosomal defects (Figures 3G–3I). This result is further supported by our previous report that *TGFB1* is one of the common mitochondrial defect signature genes identified from various mitochondrial defect models (Lee et al., 2015). Furthermore, as shown in the GSEA result in Figure 2C, TGF-β signaling was significantly enriched in H-MD. These findings raise the possibility that *TGFB1* may play a key role in mediating the effect of mitoribosomal defects within the tumor microenvironment. TGF-β signaling is known to exhibit either tumor-suppressive or oncogenic properties, depending on the tumor

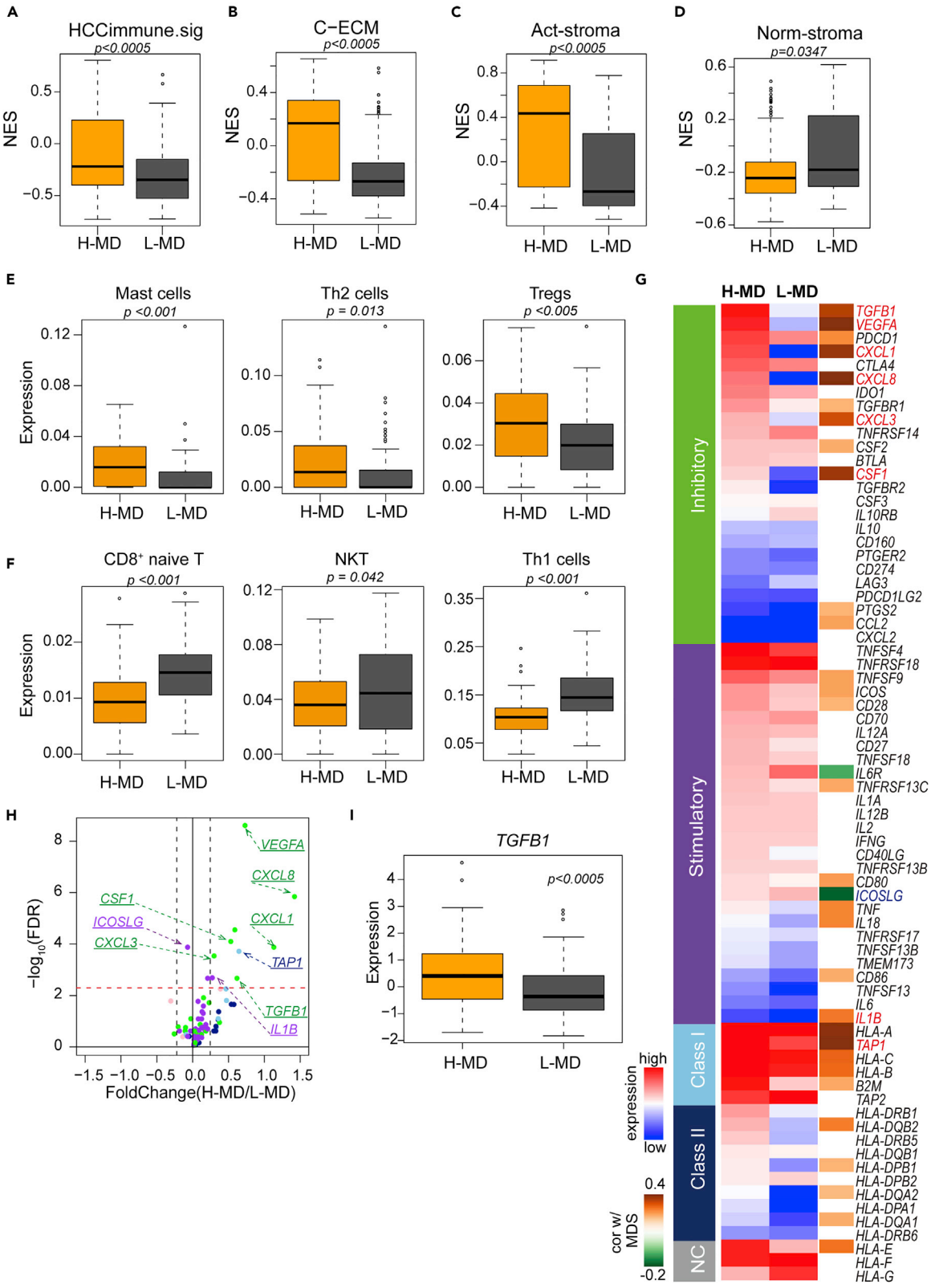
A
HCCimmune.sig
p<0.0005
NES
H-MD
L-MD
B
C−ECM
p<0.0005
C
Act-stroma
p<0.0005
D
Norm-stroma
p=0.0347
E
Mast cells
p <0.001
Th2 cells
p = 0.013
Tregs
p <0.005
Expression
F
CD8⁺ naive T
p <0.001
NKT
p = 0.042
Th1 cells
p <0.001
G
H-MD L-MD
Inhibitory
Stimulatory
Class I
Class II
NC
TGFB1
VEGFA
PDCD1
CXCL1
CTLA4
CXCL8
IDO1
TGFBR1
CXCL3
TNFRSF14
CSF2
BTLA
CSF1
TGFBR2
CSF3
IL10RB
IL10
CD160
PTGER2
CD274
LAG3
PDCD1LG2
PTGS2
CCL2
CXCL2
TNFSF4
TNFRSF18
TNFSF9
ICOS
CD28
CD70
IL12A
CD27
TNFSF18
IL6R
TNFRSF13C
IL1A
IL12B
IL2
IFNG
CD40LG
TNFRSF13B
CD80
ICOSLG
TNF
IL18
TNFRSF17
TNFSF13B
TMEM173
CD86
TNFSF13
IL6
IL1B
HLA-A
TAP1
HLA-C
HLA-B
B2M
TAP2
HLA-DRB1
HLA-DQB2
HLA-DRB5
HLA-DQB1
HLA-DPB1
HLA-DPB2
HLA-DQA2
HLA-DPA1
HLA-DQA1
HLA-DRB6
HLA-E
HLA-F
HLA-G
high
expression
low
0.4
cor w/ MDS
-0.2
H
−log10(FDR)
FoldChange(H-MD/L-MD)
VEGFA
CXCL8
CSF1
ICOSLG
CXCL3
CXCL1
TAP1
TGFB1
IL1B
I
TGFB1
p<0.0005

Figure 3. Mitoribosomal Defects Are Closely Associated with Immune Cell Response in HCC

(A–D) preRanked GSEA was performed based on the HCC immune-related signature (A), cancer-associated ECM signature (B), activated stroma-associated signature (C), and normal stroma-associated signature (D). NES for each gene set is compared between H-MD and L-MD.

(E and F) The proportion of immune cells with pro-cancer (Mast cells, Th2 cells, and T_{reg}s) (E) and with anti-cancer properties (CD8+ T cells, NK-T cells, and Th1 cells) (F) are compared between H-MD and L-MD based on the *xCell* analysis output.

(G) The average expression values of immune-modulatory cytokines in either H-MD or L-MD group are shown in colored scale. According to their immune response-related properties, cytokines were classified as inhibitory; stimulatory; MHC classes I, II, and non-classified (NC) and marked with green-, purple-, sky blue-, navy blue-, and gray-colored bars, respectively. A significant association with MDS_{dn} is shown as a colored scale, and non-significant association is shown as blank.

(H) Permutation t test was performed between H-MD and L-MD among the immune-modulatory cytokines. The x axis indicates the expression fold change between H-MD and L-MD, and the y axis indicates the $-\log_{10}$FDR for each cytokine. Cytokines significantly associated with MDS_{dn} are depicted in color coded in (G) according to their immune-related properties.

(I) *TGFB1* expression is compared between H-MD and L-MD. Boxplots are shown as first quartile, median, and third quartile (bottom box, middle line, and top box, respectively) with Welch two-sample t test p values. Whiskers represent the minimum and maximum values.

See also Figure S4 and S5; Tables S6 and S7.

stage. Moreover, HCC tissues enriched with a late-responsive TGF-β signature showed a significantly poorer prognosis with shorter mean survival time, displaying an invasive phenotype and increased tumor recurrence compared with the tissues enriched with an early responsive TGF-β signature (Coulouarn et al., 2008). Consequently, we examined the relevance of mitoribosomal defects with the early- and late-responsive TGF-β signatures. In this analysis, we found that the late TGF-β signature was more enriched in H-MD, whereas few differences in the enrichment of the early TGF-β signature were observed between subtypes (Figures S4B and S4C), indicating a close association of mitoribosomal defects with the tumor-promoting TGF-β signature. To elucidate the effect of mitoribosomal defects on the tumor microenvironment, we assessed the TGF-β responses in endothelial cells, fibroblasts, T cells, and macrophages based on the cell type-specific TGF-β response signatures (TBRS) derived from cells cultured with TGF-β (Calon et al., 2012) (i.e., E-TBRS, F-TBRS, T-TBRS, or M-TBRS). In this analysis, all the TBRS were highly enriched in the H-MD group and were strongly associated with mitoribosomal defects (Figures S4D and S4H). Furthermore, we found a robust direct correlation among them, implying their concurrent expression among samples with mitoribosomal defects to a large extent (Figure S4H). These results suggest that mitoribosomal defect-mediated TGF-β expression may be an essential regulator of various cell types in the tumor microenvironment, thereby promoting HCC progression.

Mitoribosomal Defects Regulate Immune Modulator Expression in HCC Cells

Next, to validate the involvement of mitoribosomal defects in HCC immune modulator expression, we analyzed the transcriptome data of HCC cell lines from the Cancer Cell Line Encyclopedia (CCLE) (Transparent Methods). By applying the same approach in HCC tissue samples, we inferred MDS_{dn} in cancer cell lines and categorized cancer cell lines into the H-MD type or L-MD type, respectively (Figure 4A and Table S8). First, to validate the strong association of mitoribosomal defects with immune modulators (Figure 3G), we compared their expression between H-MD and L-MD. This analysis confirmed the upregulation of *TGFB1* and colony-stimulating factor-1 (*CSF1*) and the downregulation of *ICOSLG* in H-MD-type cells (Figures 4B, 4C, and S5A). These findings suggest that they are key immune modulators mediating the immune response induced by mitoribosomal defects in HCC cells. As *CSF1* is involved in the immunosuppressive nature of the HCC microenvironment via the *SPP1*/*CSF1*/*CSF1R* axis (Zhu et al., 2019), we assessed the association of mitoribosomal defects with the CSF1 signaling axis. In addition to the upregulated expression of secreted phosphoprotein 1 (*SPP1*), the CSF1 axis was positively associated with mitoribosomal defects showing higher enrichment in H-MD-type cells (Figures 4D, 4E, and S5B). As a proof of concept, we selected two H-MD-type (JHH4 and SNU475) and two L-MD-type cell lines (HepG2 and JHH5) and confirmed the low to rare expression of a few representative down-MRPs in the H-MD-type compared with L-MD-type cells (Figure 4F). Following the unified nomenclature for MRP (De Silva et al., 2015), we used mS31 and mL46 for proteins of *MRPS31* and *MRPL46*. We further examined whether down-MRPs were truly linked to the integrity of mitoribosome. When cellular components were subjected to sucrose gradient sedimentation, JHH4 showed a lower level of mitochondrial ribosomal subunit assembly (28S small, 39S large, and 55S total subunits) compared with HepG2 (Figure 4G). The assembly profile of JHH4 was not clearly distorted, indicating overall assembly was decreased due to the low MRP expression. Moreover, the protein levels of mitochondria-encoded genes, *MT-CO2* and *MT-ND6*, were lower in the H-MD than in the L-MD type, whereas the protein level of the nuclear-encoded gene (succinate dehydrogenase complex flavoprotein subunit A; *SDHA*) was unchanged (Figure 4F). When HCC cells were exposed to MG132, which has been verified as an inhibitor of mitochondrial protein (Lavie et al., 2018), MT-COX2 level of

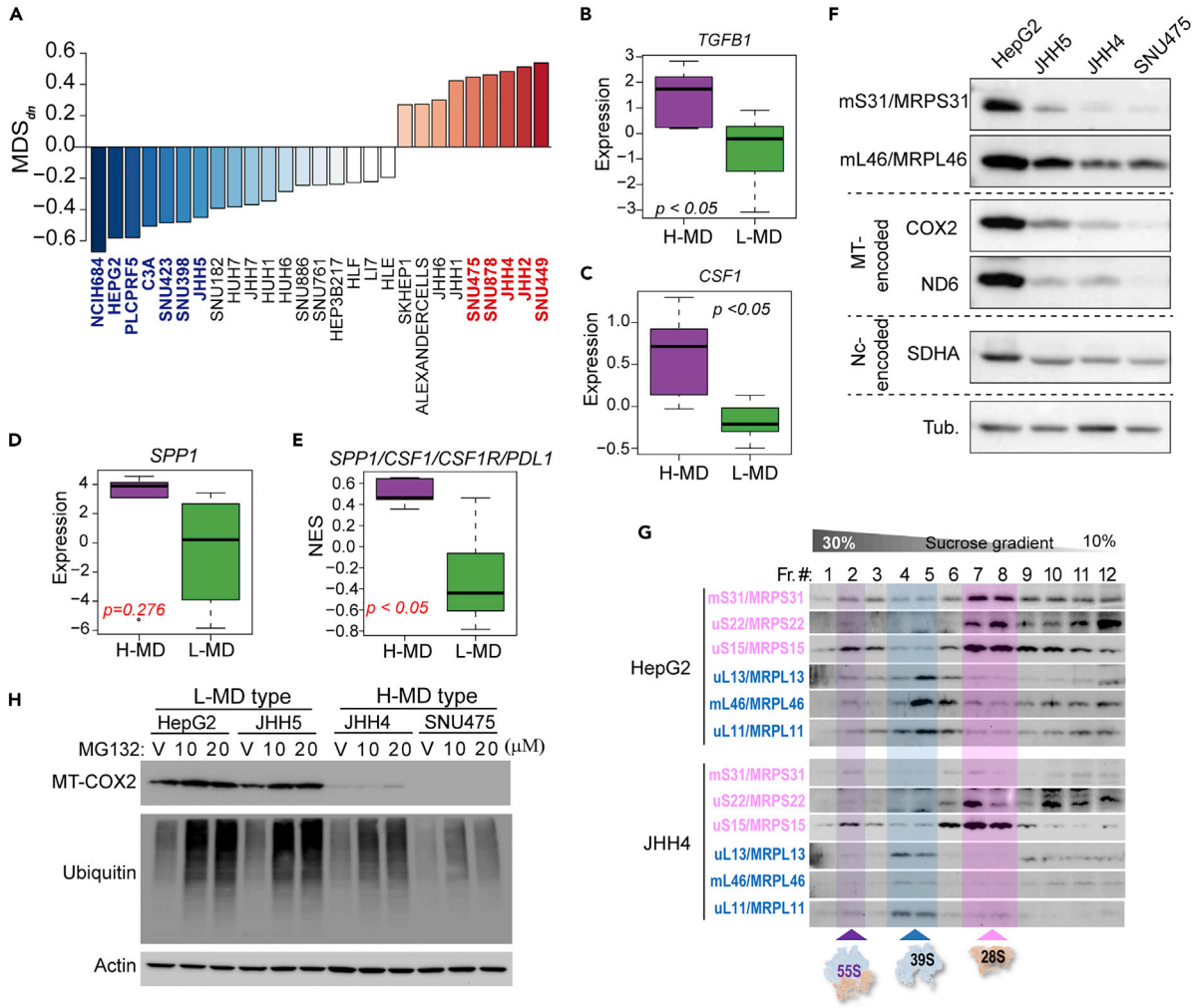
A
MDS dn
NCIH684
HEPG2
PLCPRF5
C3A
SNU423
SNU398
JHH5
SNU182
HUH7
JHH7
HUH1
HUH6
SNU886
SNU761
HEP3B217
HLF
LI7
HLE
SKHEP1
ALEXANDERCELLS
JHH6
JHH1
SNU475
SNU878
JHH4
JHH2
SNU449
B
TGFB1
Expression
p < 0.05
H-MD
L-MD
C
CSF1
Expression
p <0.05
H-MD
L-MD
D
SPP1
Expression
p=0.276
H-MD
L-MD
E
SPP1/CSF1/CSF1R/PDL1
NES
p < 0.05
H-MD
L-MD
F
HepG2
JHH5
JHH4
SNU475
mS31/MRPS31
mL46/MRPL46
MT-encoded
COX2
ND6
Nc-encoded
SDHA
Tub.
G
30%
Sucrose gradient
10%
Fr.#: 1 2 3 4 5 6 7 8 9 10 11 12
HepG2
JHH4
mS31/MRPS31
uS22/MRPS22
uS15/MRPS15
uL13/MRPL13
mL46/MRPL46
uL11/MRPL11
55S
39S
28S
H
L-MD type
H-MD type
HepG2
JHH5
JHH4
SNU475
MG132: V 10 20 V 10 20 V 10 20 V 10 20 (μM)
MT-COX2
Ubiquitin
Actin
I
TGFB1
mRNA expression (%)
HepG2
JHH5
JHH4
SNU475
J
CSF1
mRNA expression (%)
HepG2
JHH5
JHH4
SNU475
K
HepG2
Doxy (μg/ml) 0 5 10 20 40 0
MT-encoded
COX2
ND6
Nc-encoded
SDHA
Actin
L
HepG2
TGFB1 mRNA (%)
Doxy (μg/ml)
M
HepG2
CSF1 mRNA (%)
Doxy (μg/ml)
N
JHH5
Doxy (μg/ml) 0 0.625 1.25 2.5 5.0 0
MT-encoded
COX2
ND6
Nc-encoded
SDHA
Actin
O
JHH5
TGFB1 mRNA (%)
Doxy (μg/ml)
P
JHH5
CSF1 mRNA (%)
Doxy (μg/ml)

Figure 4. Mitoribosomal Defects Regulate HCC Immune Modulator Expression in HCC Cells

For validation in the HCC cell lines, transcriptome data for HCC cell line was obtained from CCLE dataset. MDS_{dn} for each HCC cell line was calculated (Methods).

(A) According to the increasing order of MDS_{dn}, MDS_{dn} of each HCC cell line is plotted. HCC cell lines representing H-MD or L-MD subgroup are marked in red or blue color, respectively.

(B–E) Messenger RNA expression of *TGFB1* (B), *CSF1* (C), and SPP1 (D) are compared between H-MD-type and L-MD-type HCC cell lines of (A). The preRanked GSEA was performed based on the *SPP1/CSF1/CSF1R/PDL1* signal axis, which is related to a sensitivity of anti-PD-1 immunotherapy in patients with HCC (E). The NES was compared between D- and ND-type cell lines (E). Boxplots are shown as first quartile, median, and third quartile (bottom box, middle line, and top box, respectively) with Welch two-sample t test p values. Whiskers represent the minimum and maximum values.

(F) Protein levels of Dn-MRPs (*MRPS31* and *MRPL46*) and mitochondrial-encoded genes (*MT-CO2* and *MT-ND6*) were validated in representative H-MD-type (JHH4 and SNU475) and L-MD-type cell line (HepG2 and JHH5) by western blot. According to new nomenclature for mitoribosomal protein, we used mS31 and mL46 for proteins of *MRPS31*and *MRPL46*.

(G) Sucrose gradient sedimentation analysis of MRPs from whole-cell lysates of the indicated cell lines. According to the new nomenclature for mitoribosomal protein, we used mS31, uS22, uS15, uL15, uL13, uL11, and mL46 for proteins of *MRPS31*, *MRPS22*, *MRPS15*, *MRPL13*, *MRPL11*, and *MRPL46*.

(H) HCC cells were exposed to various doses of MG132 for 12 h and subjected to western blot analysis. DMSO was used as a vehicle (V).

(I and J) Messenger RNA expression of *TGFB1* (I) and *CSF1* (J) in two H-MD-type (JHH4 and SNU475) and two L-MD-type cell lines (HepG2 and JHH5) were monitored by qRT-PCR.

(K–P) L-MD-type cell lines (HepG2 and JHH5) were exposed to various doses of mitochondria-specific translation inhibitor, doxycycline (DOX) for 72 h. JHH5 cells showed higher sensitivity to DOX than HepG2. Western blot analysis for the expression level of mtDNA-encoded proteins, COX2 and ND6, and nuclear DNA-encoded SDHA protein was also examined to prove the inhibitor's specificity (K and N). Messenger RNA expression of *TGFB1* (L and O) and *CSF1* (M and P) were examined by qRT-PCR. Bar plots are represented as mean ± SEM. *$p < 0.05$, **$p < 0.01$, ***$p < 0.005$ (Student's t test, DOX treated group versus non-treated group).

See also Table S8.

H-MD-type cells was not restored to the basal level of L-MD-type cells, whereas that of the L-MD-type cell was further augmented (Figure 4H). These results indicate that the two H-MD-type cell lines support a decreased mitochondria-specific translational capacity, which is associated with mitoribosomal defects, rather than weak protein stability. We further validated that the two H-MD-type HCC cells, JHH4 and SNU475, harbored increased *TGFB1* and *CSF1* mRNA levels, compared with the L-MD-type cells (Figures 4I and 4J). When L-MD-type cell lines, HepG2 and JHH5, were exposed to doxycycline, which is a mitoribosome-specific translation inhibitor, the mtDNA-encoded protein expression of COX2 and ND6 was effectively decreased. However, *TGFB1* and *CSF1* mRNAs were significantly increased (Figures 4K–4P). These results clearly indicate that mitoribosomal defects in HCC cells themselves induce the expression and release of *TGFB1* and *CSF1*, suggesting their crucial involvement in fostering an immune-suppressive environment.

TBRS Induced by MRP Defects Mediates an Aggressive Phenotype in HCC

Besides suppressing the immune response, TBRS modulates cancer cell activity mainly through EMT in HCC (Chen et al., 2019; Reichl et al., 2012). Therefore, we evaluated the association of TBRS with mitoribosomal defects in HCC cells. When the TBRS of epithelial cells (Padua et al., 2008) was applied to the transcriptome data of HCC cells, mitoribosomal defects showed a strong association with TBRS, as corroborated by the increased enrichment of TBRS in H-MD-type than L-MD-type cells (Figures 5A and 5B). We also found that among the common HCC molecular subclass described by Hoshida et al. (2009) (Hoshida et al., 2009), mitoribosomal defects had a strong positive association with the S1 subtype, yet negative associations with both the S2 and the S3 signatures (Figure 5C). These findings suggest that mitoribosomal defects are selectively associated with the molecular features of the S1 subtype. As vascular invasion is a well-defined clinical feature for the S1 subtype, we assessed the association of mitoribosomal defects with an invasive signature from a multi-cancer study (Anastassiou et al., 2011). Consistently, mitoribosomal defects were positively associated with cancer cell invasiveness (Figure 5D). Furthermore, invasive features were highly enriched in H-MD-type cells (Figure 5E). To examine whether the invasion ability of HCC cells was influenced by mitoribosomal defect-mediated TGF-β signaling, we implemented the invasion assay using H-MD-type cells (JHH4 and SNU475) and L-MD-type (HepG2 and JHH5) HCC cells. H-MD-type cells showed higher invasion activity than L-MD-type cells despite their delayed cell growth rate (Figures 5F and 5G). When we incubated H-MD-type cells with culture medium containing TGF-β-neutralizing antibodies to block TGF-β signaling, TBRS was effectively abrogated as evidenced by decreased Smad2 phosphorylation (Figures 5H and 5I). This indicated that H-MD-type cells truly released TGF-β and that their TBRS was active. Moreover, we found that the invasion capacity of H-MD-type cells was significantly reduced by eliminating TBRS (Figures 5J and 5K). These results indicate that mitoribosomal defect-mediated TGF-β release regulated the invasion activity of H-MD-type cells in an autocrine manner.

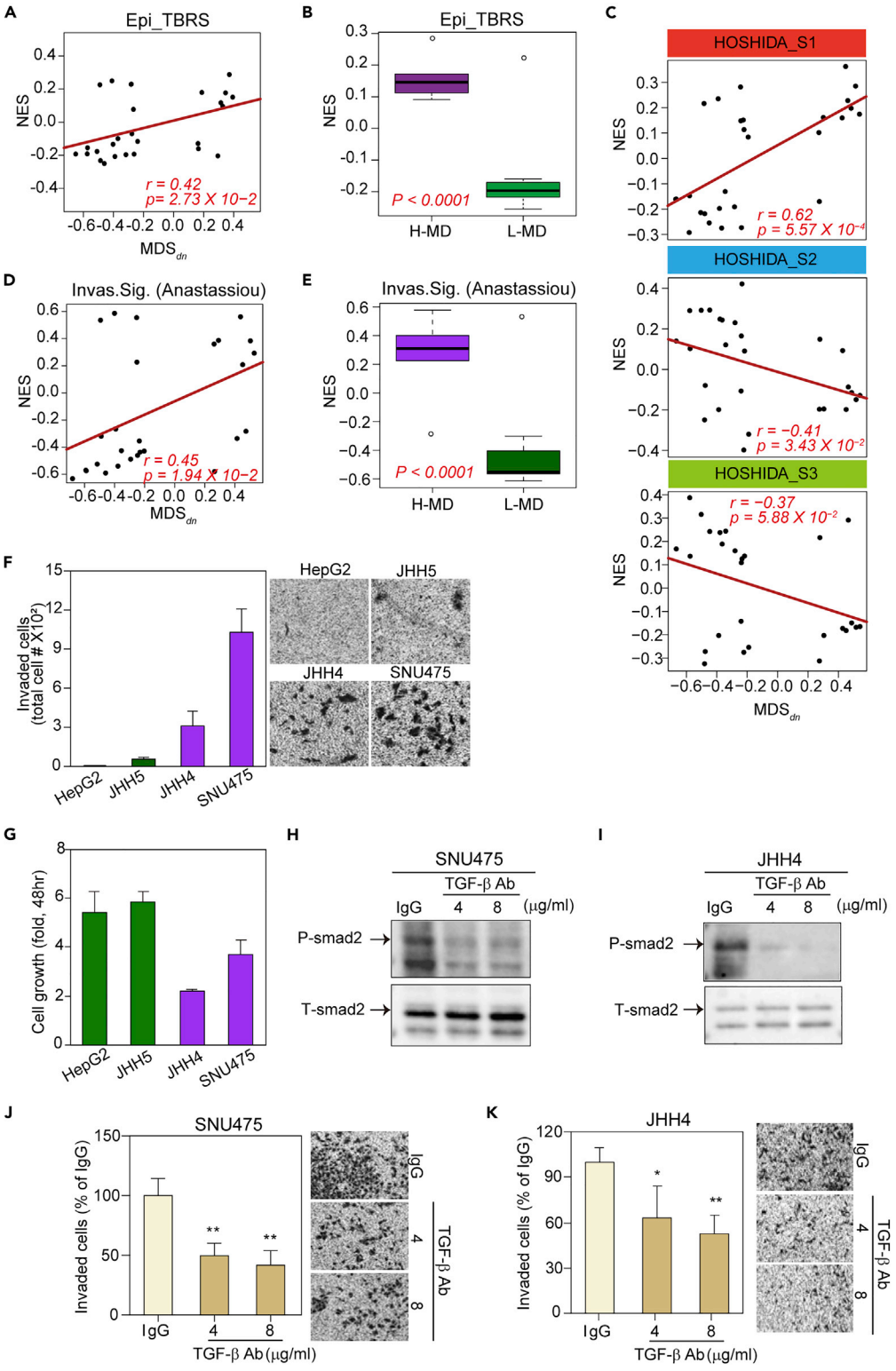

Figure 5. TBRS Induced by MRP Defects Mediates an Aggressive Phenotype in HCC

(A and B) The association of mitoribosomal defects in HCC with TBRS was recapitulated in HCC cell lines. For TBRS in HCC cell line, signatures of epithelial cells (Epi_TBRS) were used. The MDS_{dn} shows a significant correlation with Epi_TBRS (A). NES based on Epi_TBRS was compared between H-MD- and L-MD-type HCC cell lines (B).

Figure 5. *Continued*

(C) MDS_{dn} shows differential associations with HCC sub-classification signatures (Hoshida_S1, S2, and S3).

(D and E) The association of mitoribosomal defect with cancer cell invasiveness was examined. preRanked GSEA was performed based on the invasion signature defined by Anastassiou et al. MDS_{dn} shows a significant association with cancer cell invasiveness (D). NES based on cancer cell invasiveness signature (Anastassiou et al.) was compared between H-MD and L-MD-type HCC cell lines (E).

(F) Cell invasion activity was assayed using Matrigel-coated Transwell as described in the Transparent Methods section. Representative images are shown in the right panel.

(G) Cell growth rates were monitored by counting the trypan blue-negative viable cells using the Countess automated cell counter.

(H–K) TGF-β signaling in H-MD-type HCC cell lines (SNU475 and JHH4) was abolished by exposure to various concentrations of neutralizing antibodies for TGF-β (GTX14052, GeneTex Inc., Irvine, CA) for 24 h. Normal mouse IgG (sc-2025, Santa Cruz Biotechnology, Inc., Dallas, TX) was used as control. Phosphorylated SMAD2 (P-smad2) and total SMAD2 (T-smad2) levels were examined by western blot to validate the extent of TGF-β signaling inhibition (H and I). Then, the cell invasion assay was performed (J and K). Representative images for invaded cells are shown in the right panels.

Boxplots are shown as first quartile, median, and third quartile (bottom box, middle line, and top box, respectively) with Welch two-sample t test p values. Whiskers represent the minimum and maximum values. Bar plots are represented as mean ± SEM. *p<0.05, **p<0.01, ***p<0.005 (Student's t-test, DOX treated group vs. non-treated group).

See also Figure S6; Table S9.

Last, we postulated that the mitoribosomal defect-mediated invasion capacity of H-MD-type cells was also closely linked with HCC recurrence. To test this hypothesis, we performed GSEA using HCC recurrence signatures (Woo et al., 2008; Hoshida et al., 2008; Iizuka et al., 2003; Yoshioka et al., 2009; Kurokawa et al., 2004) and examined their association with mitoribosomal defects (Table S8). Based on the upregulated or downregulated genes in the recurred HCC samples from Woo et al. (2008) and Hoshida et al. (2008), we investigated the association of mitoribosomal defects with HCC recurrence. In this analysis, the H-MD subtype showed increased enrichment of upregulated genes and decreased enrichment of downregulated genes, indicating that mitoribosomal defects in HCC cells were strongly associated with HCC recurrence (Table S9 and Figures S6A–S6D). Although early recurrence was one of the clinical features of the S1 subtype (Hoshida et al., 2009), there was no significant association of early recurrence signatures with mitoribosomal defects (Table S9 and Figures S6E and S6F). Considering that the distinct genetic features were involved in the early and late recurrence of HCC, these results implied that mitoribosomal defects were selectively associated with molecular features of late recurring HCC.

Taken together, these results indicate that the mitoribosomal defects caused by aberrant expression of down-MRPs are one of the causes of OXPHOS impairment and the related overall mitochondrial dysfunction, further introducing a novel mitochondria-related HCC hallmark. Also, our findings demonstrate that mitoribosomal defects actively participate in establishing a favorable microenvironment by recruiting suppressive immune cells and activating the ECM to increase the invasion capacity of tumor cells. In detail, the TGF-β signaling pathway is a crucial mechanism to mediate mitoribosomal defects with the diverse aggressive molecular features of HCC. This implies that a set of down-MRPs may be used as good prognostic markers for HCC and that therapeutics co-targeting TGF-β and down-MRPs can be a more selective strategy for the treatment of HCC with mitoribosomal defects.

DISCUSSION

As a specialized mitochondrial translational machinery, the mitoribosome integrity is essential for OXPHOS function including ATP production in an aerobic manner. Thus, aberrant expression of the MRPs comprising mitoribosomes may result in critical defects in energy production and in the overall regulation of cellular respiration, further resulting in deregulated cellular energetics, which has recently been added as a cancer hallmark (Hanahan and Weinberg, 2011). There are several underlying mechanisms such as mtDNA mutations, mitochondrial enzyme defects, or altered oncogenes/tumor suppressors explaining the close association of mitochondrial dysfunction with deregulated cellular energetics (Wallace, 2012; Cairns et al., 2011). However, to date, the contribution of mitoribosomal defects on deregulated cellular energetics has not been studied well. Moreover, metabolic reprogramming in hepatocytes has been proposed as a key component in the progression to malignant HCC cells (Cancer Genome Atlas Research Network. Electronic address and Cancer Genome Atlas Research Network, 2017). Thus, we hypothesized that mitoribosomal defects induced by MRP aberration may contribute to the initiation and progression of HCC. To the best of our knowledge, this study is the first to systematically profile the MRPs in HCC and elucidate how mitoribosomal defects affect HCC progression. In this study, we identified a signature

reflecting mitoribosomal defects, consisting of six downregulated MRPs, MRPL39, MRPL46, MRPL34, MRPL54, MPLS6, and MPLS31, and devised a scoring metric of the mitoribosome defect using these genes and designated it as MDS. Interestingly, we found that MDS had close associations with not only essential mitochondrial functions such as OXPHOS but also aggressive phenotypes such as the cell cycle and EMT. Moreover, MDS also had prognostic significance in indicating shorter overall survival time. These results demonstrated that the MDS could reflect the oncogenic potential of mitoribosomal defect. In addition, the differential associations of MDS with infiltrated immune cells, associations such as higher MDS in the tumor showed increased enrichment with immune cells having suppressive characteristics and less enrichment with immune cells having stimulatory characteristics, indicated that mitoribosomal defects attract a differential repertoire of immune cells and provide a favorable microenvironment for cancer cells by recruiting immune cells with suppressive activity and promoting escape from immune surveillance.

Among suppressive cytokines, *TGFB1* showed a significant association with mitoribosomal defects as *in vitro* analysis using the H-MD-type and L-MD-type HCC cell lines showed increased *TGFB1* expression in the H-MD type and mitoribosome defect-induced TBRS activation affected cancer cell invasion. Based on our findings, we postulate that *TGFB1* plays a crucial role in constructing a favorable microenvironment that is induced by the mitoribosomal defects. As a pleiotropic cytokine, TGF-β regulates cellular proliferation, differentiation, and ECM production. Aberrant expression of TGF-β or dysregulated TBRS has been involved in the pathogenesis of a variety of diseases, including cancer and fibrosis. Moreover, TGF-β was elevated in both the plasma and tumor tissues of patients with HCC (Giannelli et al., 2002), and TBRS activation was considered to engage in hepatocarcinogenesis and to contribute to EMT in HCC models (Giannelli et al., 2005). Interestingly, Yi et al. recently reported a direct association between TGF-β with mitochondrial dysfunction in HCC, demonstrating that *TGFB1* expression was augmented in mitochondria-depleted ρ0 HCC cell lines and that TBRS was involved in the EMT induced by mitochondrial dysfunction (Yi et al., 2015). In addition, a recent study using human peripheral and tumor-associated lymphocytes, tumor-derived TGF-β, demonstrated the suppression of a key antitumor function of $CD4^+$ T cells and interferon-γ production by inhibiting the mitochondrial respiration (Dimeloe et al., 2019). Considering these findings, we suggest TGF-β as a key effector mediating the effect of mitoribosomal defect on HCC progression and immune evasion.

However, we could not clearly present how mitoribosome defects in HCC upregulate the expression of *TGFB1* and activate TBRS, or clarify how activated TBRS fosters a cancer-favorable microenvironment and suppresses anti-tumor immunity. One plausible explanation for this can be the rise of mitochondrial ROS as a result of OXPHOS dysfunction in mitoribosome-defective HCC. Furthermore, Jain et al. reported that mitochondrial ROS regulated TBRS and augmented TGF-β-mediated transcription in primary normal human lung fibroblasts (Jain et al., 2013). Depending on their concentration and cellular compartmentalization, ROS behave ambivalently in cancer progression. ROS facilitate carcinogenesis and cancer progression under mild-to-moderate elevated levels, whereas excessive ROS damages cancer cells dramatically, causing cell death (Zhang et al., 2016; Tafani et al., 2016). Furthermore, as signaling messengers in the immune system, ROS are associated with tumor-induced immunosuppression in the tumor microenvironment by extensively participating in T cell activation, apoptosis, and hyporesponsiveness. Owing to this, we consider that ROS evoked from the mitoribosomal defects may play a crucial function in the suppressive immunity of the cancer microenvironment via TBRS. Meanwhile, TGF-β, which can promote ROS generation in the mitochondria of damaged hepatocytes, has been reported by directly downregulating antioxidative systems (Albright et al., 2003). In this way, both TGF-β and ROS are building a strong interaction that provides an advantage to cancer cells to increment their malignancy. The mutual collaboration of TGF-β and ROS in mitoribosomal defect may be difficult to probe, due to their inherently complex and contradictory role in cancer progression (Krstic et al., 2015).

Although it is not clear how mitoribosome defects in HCC foster a cancer-favorable microenvironment and suppress anti-tumor immunity, we found that *SPP1*, *CSF1*, as well as *TGFB1* was highly enriched in the mitoribosome-defective tumor. Furthermore, activation of the *SPP1*/*CSF1*/*CSF1R* axis has been reported to provide the immunosuppressive nature of the HCC microenvironment and to be correlated with the increased expression of programmed cell death protein 1 (PD-1) (Zhu et al., 2019). Furthermore, the expression level of PD-1 is correlated with cellular ROS production and oxidative metabolism (Tkachev et al., 2015). PD-1 is considered an immune checkpoint that controls T cell function, and the high expression of PD-1 is currently under investigation as a potential predictor of responses to anti-PD1 therapy (Herbst

et al., 2016; Garon et al., 2015; Topalian et al., 2012). As PD-1 maintains immune homeostasis by negatively regulating T cell function and survival, PD-1 blockade has been recently approved to treat patients with advanced-stage cancers by enhancing antitumor T cell immunity (Tan and Quintal, 2015). Furthermore, TGF-β inhibitors showed promise in several preclinical *in vitro* and *in vivo* studies (Faivre et al., 2019). Therefore, it would be interesting to stratify patients with HCC based on the magnitude of mitoribosomal defects and to explore the potential of combining ROS scavengers or TGF-β inhibitors with PD-1 signaling blockade for rapid clinical translation. Collectively, our findings demonstrate that mitoribosomal defect assessment may facilitate a survey of liver tumor immunity and stratification of patients for immune-based therapy.

Limitations of the Study

In this study, we could not present the precise underlying mechanism of how mitoribosome defects in HCC upregulate the expression of *TGFB1* and activate TBRS. Also, we could not clarify how activated TBRS fosters a cancer-favorable microenvironment and suppresses anti-tumor immunity.

Resource Availability

Lead Contact

Further information and requests for resources and reagents should be directed to and will be fulfilled by Lead Contact, So Mee Kwon (smkwon@ajou.ac.kr)

Material Availability

This study did not generate new unique reagents. RNA sequencing data for TCGA liver cancer cohorts and HCC cell lines were obtained from Genomic Data Commons Data portal (https://docs.gdc.cancer.gov) and CCLE (Cancer Cell Line Encyclopedia, https://portals.broadinstitute.org/ccle).

Data and Code Availability

No previously unreported algorithms were used to generate the results.

METHODS

All methods can be found in the accompanying Transparent Methods supplemental file.

SUPPLEMENTAL INFORMATION

Supplemental Information can be found online at https://doi.org/10.1016/j.isci.2020.101247.

ACKNOWLEDGMENTS

This work was supported by the National Research Foundation of Korea (NRF) grant funded by the Ministry of Science and ICT (MSIT) (G.Y., NRF-2015R1A2A1A10055038; H.G.W., NRF-2017R1E1A1A01074733 and NRF-2017M3A9B6061509) and also supported by a fellowship from the Basic Science Research Program through the NRF grant funded by the Ministry of Education (S.M.K., NRF-2017R1A6A3A11030191).

AUTHOR CONTRIBUTIONS

S.M.K and G.Y. conceived the idea. S.M.K. carried out most of the data analysis. Y.-K.L. and S.M. performed all experiments. H.G.W. and H.J.W advised data analysis approaches. S.M.K., H.G.W., and G.Y. interpreted data and prepared the manuscript. All authors read, advised, and approved the manuscript.

DECLARATION OF INTERESTS

The authors declare no competing interests.

Received: January 10, 2019
Revised: April 30, 2020
Accepted: June 3, 2020
Published: June 26, 2020

REFERENCES

Albright, C.D., Salganik, R.I., Craciunescu, C.N., Mar, M.H., and Zeisel, S.H. (2003). Mitochondrial and microsomal derived reactive oxygen species mediate apoptosis induced by transforming growth factor-beta1 in immortalized rat hepatocytes. J. Cell Biochem *89*, 254–261.

Anastassiou, D., Rumjantseva, V., Cheng, W., Huang, J., Canoll, P.D., Yamashiro, D.J., and Kandel, J.J. (2011). Human cancer cells express Slug-based epithelial-mesenchymal transition gene expression signature obtained in vivo. BMC Cancer *11*, 529.

Aran, D., Hu, Z., and Butte, A.J. (2017). xCell: digitally portraying the tissue cellular heterogeneity landscape. Genome Biol. *18*, 220.

Auger, C., Alhasawi, A., Contavadoo, M., and Appanna, V.D. (2015). Dysfunctional mitochondrial bioenergetics and the pathogenesis of hepatic disorders. Front. Cell Dev Biol *3*, 40.

Cairns, R.A., Harris, I.S., and Mak, T.W. (2011). Regulation of cancer cell metabolism. Nat. Rev. Cancer *11*, 85–95.

Caja, L., Dituri, F., Mancarella, S., Caballero-Diaz, D., Moustakas, A., Giannelli, G., and Fabregat, I. (2018). TGF-beta and the tissue microenvironment: relevance in fibrosis and cancer. Int. J. Mol. Sci. *19*, 1294–1317.

Calon, A., Espinet, E., Palomo-Ponce, S., Tauriello, D.V., Iglesias, M., Cespedes, M.V., Sevillano, M., Nadal, C., Jung, P., Zhang, X.H., et al. (2012). Dependency of colorectal cancer on a TGF-beta-driven program in stromal cells for metastasis initiation. Cancer Cell *22*, 571–584.

Cancer Genome Atlas Research Network. Electronic address: wheeler@bcm.edu; Cancer Genome Atlas Research Network. (2017). Comprehensive and Integrative Genomic Characterization of Hepatocellular Carcinoma. Cell *169*, 1327–1341.e23.

Carim, L., Sumoy, L., Nadal, M., Estivill, X., and Escarceller, M. (1999). Cloning, expression, and mapping of PDCD9, the human homolog of Gallus gallus pro-apoptotic protein p52. Cytogenet. Cell Genet. *87*, 85–88.

Chakravarthy, A., Khan, L., Bensler, N.P., Bose, P., and De Carvalho, D.D. (2018). TGF-beta-associated extracellular matrix genes link cancer-associated fibroblasts to immune evasion and immunotherapy failure. Nat. Commun. *9*, 4692.

Chandra, D., and Singh, K.K. (2011). Genetic insights into OXPHOS defect and its role in cancer. Biochim. Biophys. Acta *1807*, 620–625.

Chen, J., Gingold, J.A., and Su, X. (2019). Immunomodulatory TGF-beta signaling in hepatocellular carcinoma. Trends Mol. Med. *25*, 1010–1023.

Chintharlapalli, S.R., Jasti, M., Malladi, S., Parsa, K.V., Ballestero, R.P., and Gonzalez-Garcia, M. (2005). BMRP is a Bcl-2 binding protein that induces apoptosis. J. Cell Biochem. *94*, 611–626.

Colegio, O.R., Chu, N.Q., Szabo, A.L., Chu, T., Rhebergen, A.M., Jairam, V., Cyrus, N., Brokowski, C.E., Eisenbarth, S.C., Phillips, G.M., et al. (2014). Functional polarization of tumour-associated macrophages by tumour-derived lactic acid. Nature *513*, 559–563.

Coulouarn, C., Factor, V.M., and Thorgeirsson, S.S. (2008). Transforming growth factor-beta gene expression signature in mouse hepatocytes predicts clinical outcome in human cancer. Hepatology *47*, 2059–2067.

De Silva, D., Tu, Y.T., Amunts, A., Fontanesi, F., and Barrientos, A. (2015). Mitochondrial ribosome assembly in health and disease. Cell Cycle *14*, 2226–2250.

Degli Esposti, D., Hamelin, J., Bosselut, N., Saffroy, R., Sebagh, M., Pommier, A., Martel, C., and Lemoine, A. (2012). Mitochondrial roles and cytoprotection in chronic liver injury. Biochem. Res. Int. *2012*, 387626.

Dimeloe, S., Gubser, P., Loeliger, J., Frick, C., Develioglu, L., Fischer, M., Marquardsen, F., Bantug, G.R., Thommen, D., Lecoultre, Y., et al. (2019). Tumor-derived TGF-beta inhibits mitochondrial respiration to suppress IFN-gamma production by human CD4(+) T cells. Sci. Signal. *12*, eaav3334.

Faivre, S., Santoro, A., Kelley, R.K., Gane, E., Costentin, C.E., Gueorguieva, I., Smith, C., Cleverly, A., Lahn, M.M., Raymond, E., et al. (2019). Novel transforming growth factor beta receptor I kinase inhibitor galunisertib (LY2157299) in advanced hepatocellular carcinoma. Liver Int. *39*, 1468–1477.

Garon, E.B., Rizvi, N.A., Hui, R., Leighl, N., Balmanoukian, A.S., Eder, J.P., Patnaik, A., Aggarwal, C., Gubens, M., Horn, L., et al. (2015). Pembrolizumab for the treatment of non-small-cell lung cancer. N. Engl. J. Med. *372*, 2018–2028.

Giannelli, G., Bergamini, C., Fransvea, E., Sgarra, C., and Antonaci, S. (2005). Laminin-5 with transforming growth factor-beta1 induces epithelial to mesenchymal transition in hepatocellular carcinoma. Gastroenterology *129*, 1375–1383.

Giannelli, G., Fransvea, E., Marinosci, F., Bergamini, C., Colucci, S., Schiraldi, O., and Antonaci, S. (2002). Transforming growth factor-beta1 triggers hepatocellular carcinoma invasiveness via alpha3beta1 integrin. Am. J. Pathol. *161*, 183–193.

Hanahan, D., and Weinberg, R.A. (2011). Hallmarks of cancer: the next generation. Cell *144*, 646–674.

Herbst, R.S., Baas, P., Kim, D.W., Felip, E., Perez-Gracia, J.L., Han, J.Y., Molina, J., Kim, J.H., Arvis, C.D., Ahn, M.J., et al. (2016). Pembrolizumab versus docetaxel for previously treated, PD-L1-positive, advanced non-small-cell lung cancer (KEYNOTE-010): a randomised controlled trial. Lancet *387*, 1540–1550.

Hoshida, Y., Nijman, S.M., Kobayashi, M., Chan, J.A., Brunet, J.P., Chiang, D.Y., Villanueva, A., Newell, P., Ikeda, K., Hashimoto, M., et al. (2009). Integrative transcriptome analysis reveals common molecular subclasses of human hepatocellular carcinoma. Cancer Res. *69*, 7385–7392.

Hoshida, Y., Villanueva, A., Kobayashi, M., Peix, J., Chiang, D.Y., Camargo, A., Gupta, S., Moore, J., Wrobel, M.J., Lerner, J., et al. (2008). Gene expression in fixed tissues and outcome in hepatocellular carcinoma. N. Engl. J. Med. *359*, 1995–2004.

Iizuka, N., Oka, M., Yamada-Okabe, H., Nishida, M., Maeda, Y., Mori, N., Takao, T., Tamesa, T., Tangoku, A., Tabuchi, H., et al. (2003). Oligonucleotide microarray for prediction of early intrahepatic recurrence of hepatocellular carcinoma after curative resection. Lancet *361*, 923–929.

Jain, M., Rivera, S., Monclus, E.A., Synenki, L., Zirk, A., Eisenbart, J., Feghali-Bostwick, C., Mutlu, G.M., Budinger, G.R., and Chandel, N.S. (2013). Mitochondrial reactive oxygen species regulate transforming growth factor-beta signaling. J. Biol. Chem. *288*, 770–777.

Khalaf, A.M., Fuentes, D., Morshid, A.I., Burke, M.R., Kaseb, A.O., Hassan, M., Hazle, J.D., and Elsayes, K.M. (2018). Role of Wnt/beta-catenin signaling in hepatocellular carcinoma, pathogenesis, and clinical significance. J. Hepatocell Carcinoma *5*, 61–73.

Koc, E.C., Haciosmanoglu, E., Claudio, P.P., Wolf, A., Califano, L., Friscia, M., Cortese, A., and Koc, H. (2015). Impaired mitochondrial protein synthesis in head and neck squamous cell carcinoma. Mitochondrion *24*, 113–121.

Krstic, J., Trivanovic, D., Mojsilovic, S., and Santibanez, J.F. (2015). Transforming growth factor-beta and oxidative stress interplay: implications in tumorigenesis and cancer progression. Oxid Med. Cell Longev. *2015*, 654594.

Kurokawa, Y., Matoba, R., Takemasa, I., Nagano, H., Dono, K., Nakamori, S., Umeshita, K., Sakon, M., Ueno, N., Oba, S., et al. (2004). Molecular-based prediction of early recurrence in hepatocellular carcinoma. J. Hepatol. *41*, 284–291.

Lavie, J., De Belvalet, H., Sonon, S., Ion, A.M., Dumon, E., Melser, S., Lacombe, D., Dupuy, J.W., Lalou, C., and Benard, G. (2018). Ubiquitin-dependent degradation of mitochondrial proteins regulates energy metabolism. Cell Rep. *23*, 2852–2863.

LeBleu, V.S., O'Connell, J.T., Gonzalez Herrera, K.N., Wikman, H., Pantel, K., Haigis, M.C., de Carvalho, F.M., Damascena, A., Domingos Chinen, L.T., Rocha, R.M., et al. (2014). PGC-1alpha mediates mitochondrial biogenesis and oxidative phosphorylation in cancer cells to promote metastasis. Nat. Cell Biol. *16*, 992–1003, 1-15.

Lee, Y.K., Jee, B.A., Kwon, S.M., Yoon, Y.S., Xu, W.G., Wang, H.J., Wang, X.W., Thorgeirsson, S.S., Lee, J.S., Woo, H.G., and Yoon, G. (2015). Identification of a mitochondrial defect gene signature reveals NUPR1 as a key regulator of liver cancer progression. Hepatology *62*, 1174–1189.

Lee, Y.K., Lim, J.J., Jeoun, U.W., Min, S., Lee, E.B., Kwon, S.M., Lee, C., and Yoon, G. (2017). Lactate-mediated mitoribosomal defects impair mitochondrial oxidative phosphorylation and

promote hepatoma cell invasiveness. J. Biol. Chem. *292*, 20208–20217.

Levy-Strumpf, N., and Kimchi, A. (1998). Death associated proteins (DAPs): from gene identification to the analysis of their apoptotic and tumor suppressive functions. Oncogene *17*, 3331–3340.

Liberzon, A., Birger, C., Thorvaldsdottir, H., Ghandi, M., Mesirov, J.P., and Tamayo, P. (2015). The Molecular Signatures Database (MSigDB) hallmark gene set collection. Cell Syst *1*, 417–425.

Loo, L.W., Cheng, I., Tiirikainen, M., Lum-Jones, A., Seifried, A., Dunklee, L.M., Church, J.M., Gryfe, R., Weisenberger, D.J., Haile, R.W., et al. (2012). cis-Expression QTL analysis of established colorectal cancer risk variants in colon tumors and adjacent normal tissue. PLoS One *7*, e30477.

Luedde, T., and Schwabe, R.F. (2011). NF-kappaB in the liver–linking injury, fibrosis and hepatocellular carcinoma. Nat. Rev. Gastroenterol. Hepatol. *8*, 108–118.

Martinez-Outschoorn, U.E., Balliet, R.M., Rivadeneira, D.B., Chiavarina, B., Pavlides, S., Wang, C., Whitaker-Menezes, D., Daumer, K.M., Lin, Z., Witkiewicz, A.K., et al. (2010). Oxidative stress in cancer associated fibroblasts drives tumor-stroma co-evolution: a new paradigm for understanding tumor metabolism, the field effect and genomic instability in cancer cells. Cell Cycle *9*, 3256–3276.

Moffitt, R.A., Marayati, R., Flate, E.L., Volmar, K.E., Loeza, S.G., Hoadley, K.A., Rashid, N.U., Williams, L.A., Eaton, S.C., Chung, A.H., et al. (2015). Virtual microdissection identifies distinct tumor- and stroma-specific subtypes of pancreatic ductal adenocarcinoma. Nat. Genet. *47*, 1168–1178.

Nunes, J.B., Peixoto, J., Soares, P., Maximo, V., Carvalho, S., Pinho, S.S., Vieira, A.F., Paredes, J., Rego, A.C., Ferreira, I.L., et al. (2015). OXPHOS dysfunction regulates integrin-beta1 modifications and enhances cell motility and migration. Hum. Mol. Genet. *24*, 1977–1990.

Padua, D., Zhang, X.H., Wang, Q., Nadal, C., Gerald, W.L., Gomis, R.R., and Massague, J. (2008). TGFbeta primes breast tumors for lung metastasis seeding through angiopoietin-like 4. Cell *133*, 66–77.

Pietromonaco, S.F., Denslow, N.D., and O'Brien, T.W. (1991). Proteins of mammalian mitochondrial ribosomes. Biochimie *73*, 827–835.

Pu, M., Wang, J., Huang, Q., Zhao, G., Xia, C., Shang, R., Zhang, Z., Bian, Z., Yang, X., and Tao, K. (2017). High MRPS23 expression contributes to hepatocellular carcinoma proliferation and indicates poor survival outcomes. Tumour Biol. *39*, 1–12.

Reichl, P., Haider, C., Grubinger, M., and Mikulits, W. (2012). TGF-beta in epithelial to mesenchymal transition and metastasis of liver carcinoma. Curr. Pharm. Des. *18*, 4135–4147.

Sia, D., Jiao, Y., Martinez-Quetglas, I., Kuchuk, O., Villacorta-Martin, C., Castro de Moura, M., Putra, J., Camprecios, G., Bassaganyas, L., Akers, N., et al. (2017). Identification of an immune-specific class of hepatocellular carcinoma, based on molecular features. Gastroenterology *153*, 812–826.

Sorensen, K.M., Meldgaard, T., Melchjorsen, C.J., Fridriksdottir, A.J., Pedersen, H., Petersen, O.W., and Kristensen, P. (2017). Upregulation of Mrps18a in breast cancer identified by selecting phage antibody libraries on breast tissue sections. BMC Cancer *17*, 19.

Sukumar, M., Kishton, R.J., and Restifo, N.P. (2017). Metabolic reprograming of anti-tumor immunity. Curr. Opin. Immunol. *46*, 14–22.

Tafani, M., Sansone, L., Limana, F., Arcangeli, T., De Santis, E., Polese, M., Fini, M., and Russo, M.A. (2016). The interplay of reactive oxygen species, hypoxia, inflammation, and sirtuins in cancer initiation and progression. Oxid Med. Cell Longev. *2016*, 3907147.

Tan, M., and Quintal, L. (2015). Pembrolizumab: a novel antiprogrammed death 1 (PD-1) monoclonal antibody for treatment of metastatic melanoma. J. Clin. Pharm. Ther. *40*, 504–507.

Tkachev, V., Goodell, S., Opipari, A.W., Hao, L.Y., Franchi, L., Glick, G.D., Ferrara, J.L., and Byersdorfer, C.A. (2015). Programmed death-1 controls T cell survival by regulating oxidative metabolism. J. Immunol. *194*, 5789–5800.

Topalian, S.L., Hodi, F.S., Brahmer, J.R., Gettinger, S.N., Smith, D.C., McDermott, D.F., Powderly, J.D., Carvajal, R.D., Sosman, J.A., Atkins, M.B., et al. (2012). Safety, activity, and immune correlates of anti-PD-1 antibody in cancer. N. Engl. J. Med. *366*, 2443–2454.

Uhlen, M., Fagerberg, L., Hallstrom, B.M., Lindskog, C., Oksvold, P., Mardinoglu, A., Sivertsson, A., Kampf, C., Sjostedt, E., Asplund, A., et al. (2015). Proteomics. Tissue-based map of the human proteome. Science *347*, 1260419.

Wallace, D.C. (2012). Mitochondria and cancer. Nat. Rev. Cancer *12*, 685–698.

Warburg, O. (1956). On the origin of cancer cells. Science *123*, 309–314.

Wei, Z., Jia, J., Heng, G., Xu, H., Shan, J., Wang, G., Liu, C., Xia, J., Zhou, H., Wu, M., et al. (2019). SIRT1/MRPS5 axis enhances the metabolic flexibility of liver cancer stem cells. Hepatology *70*, 1197–1213.

Woo, H.G., Park, E.S., Cheon, J.H., Kim, J.H., Lee, J.S., Park, B.J., Kim, W., Park, S.C., Chung, Y.J., Kim, B.G., et al. (2008). Gene expression-based recurrence prediction of hepatitis B virus-related human hepatocellular carcinoma. Clin. Cancer Res. *14*, 2056–2064.

Yi, E.Y., Park, S.Y., Jung, S.Y., Jang, W.J., and Kim, Y.J. (2015). Mitochondrial dysfunction induces EMT through the TGF-beta/Smad/Snail signaling pathway in Hep3B hepatocellular carcinoma cells. Int. J. Oncol. *47*, 1845–1853.

Yoshioka, S., Takemasa, I., Nagano, H., Kittaka, N., Noda, T., Wada, H., Kobayashi, S., Marubashi, S., Takeda, Y., Umeshita, K., et al. (2009). Molecular prediction of early recurrence after resection of hepatocellular carcinoma. Eur. J. Cancer *45*, 881–889.

Zhang, L., Li, J., Zong, L., Chen, X., Chen, K., Jiang, Z., Nan, L., Li, X., Li, W., Shan, T., et al. (2016). Reactive oxygen species and targeted therapy for pancreatic cancer. Oxid Med. Cell Longev. *2016*, 1616781.

Zhu, Y., Yang, J., Xu, D., Gao, X.M., Zhang, Z., Hsu, J.L., Li, C.W., Lim, S.O., Sheng, Y.Y., Zhang, Y., et al. (2019). Disruption of tumour-associated macrophage trafficking by the osteopontin-induced colony-stimulating factor-1 signalling sensitises hepatocellular carcinoma to anti-PD-L1 blockade. Gut *68*, 1653–1666.

Zong, W.X., Rabinowitz, J.D., and White, E. (2016). Mitochondria and cancer. Mol. Cell *61*, 667–676.

iScience, Volume *23*

Supplemental Information

Mitoribosome Defect in Hepatocellular Carcinoma Promotes an Aggressive Phenotype with Suppressed Immune Reaction

So Mee Kwon, Young-Kyoung Lee, Seongki Min, Hyun Goo Woo, Hee Jung Wang, and Gyesoon Yoon

Supplemental Figures

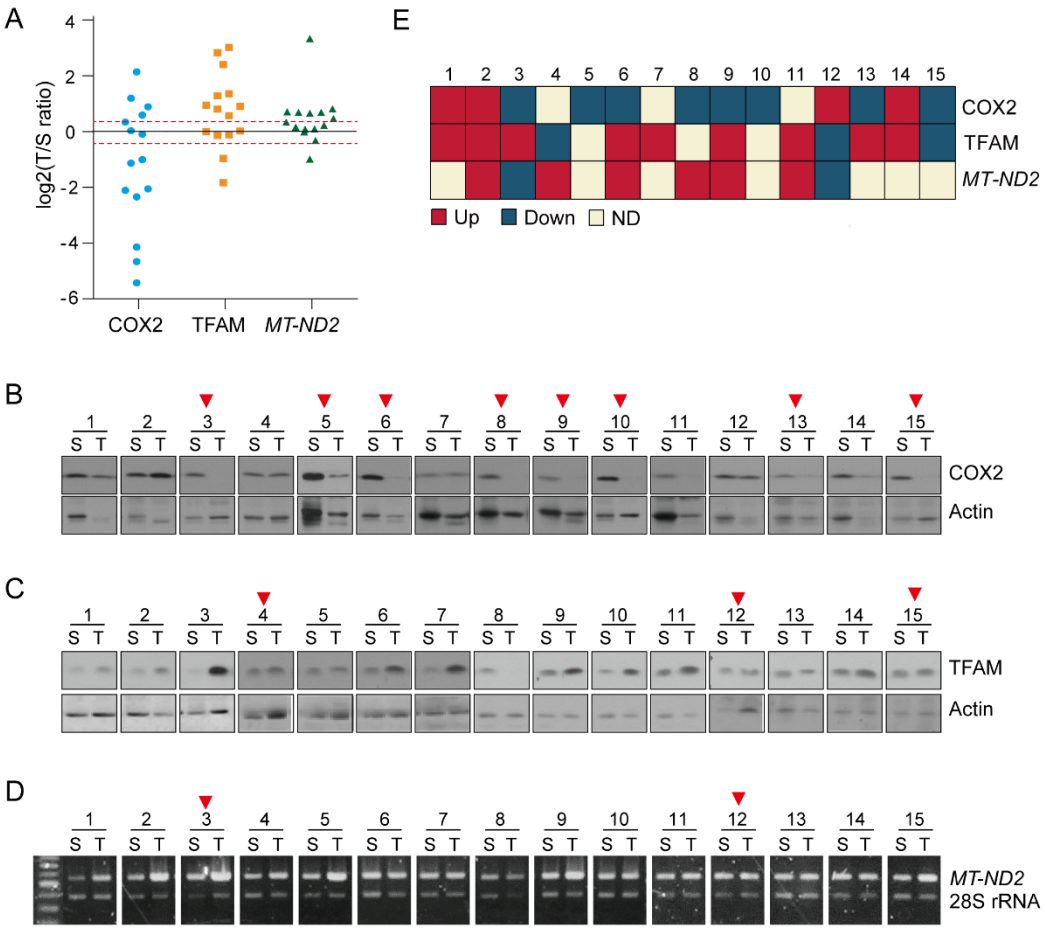

Figure S1. Comparison of mitochondrial biogenesis between paired tumor (T) and surrounding tumor tissue (S) of HCC patients, Related to Figure 1 In 15 HCC patients, mitochondrial biogenesis (i.e., mitochondrial translation, replication, and DNA copy number) between paired T and S were compared using COX2, TFAM, and *MT-ND2,* respectively. (A) The log2 ratio of T versus S for the protein of COX2 and TFAM and DNA copy number of *MT-ND2* were shown. The dotted line indicates the cut-off (0.5 or -0.5). (B-D) The western blots for COX2 (B) and TFAM (C) and PCR for DNA copy number of *MT-ND2* (D) of paired T and S of 15 HCC patients are shown. Samples were labeled as numbers (1~15). The inverted red-colored triangle indicates that the level in T is lower than in S. (E) Based on the cut-off in (A), log2 ratio of T versus S for COX2, TFAM, and MT-ND2 in each sample was assigned into Up (>0.5), Down(< -0.5), or ND (-0.5< <0.5).

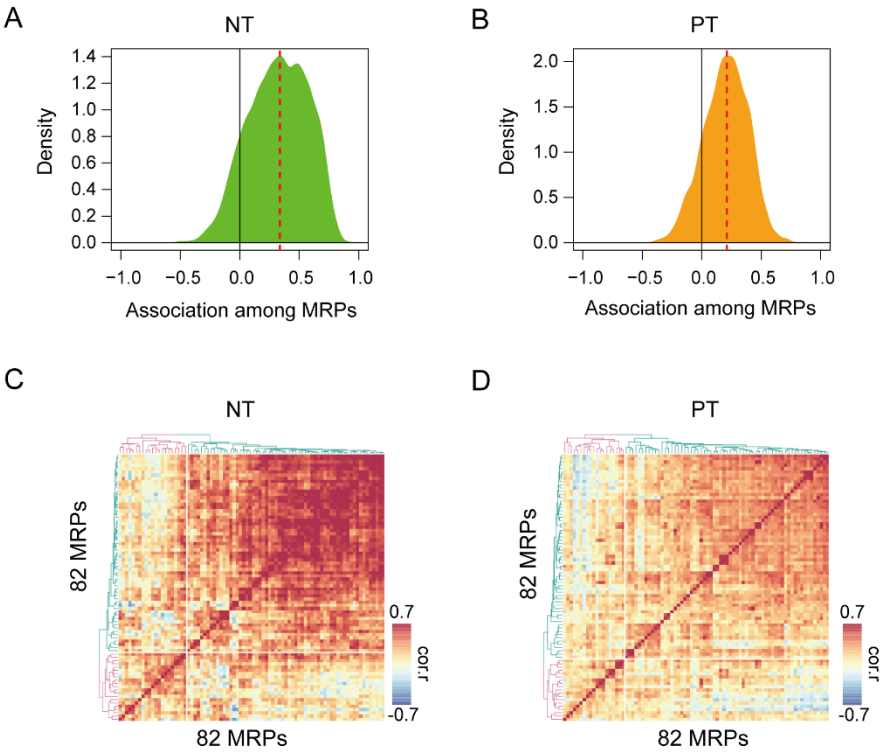

Figure S2. Association among 82 MRPs of the primary tumor (PT) and non-tumor (NT) of TCGA HCC cohort, Related to Figure 1C-D (A-D) The association among 82 MRPs in PT (n=371) and NT (n=50) was estimated. The histogram indicates the density of correlation estimates of NT(A) or PT (B). Correlation plot indicates the strength of association among MRPs. Correlation estimates are shown in colored scales, respectively.

Figure S3. Comparison of enrichment of gene sets associated with H-MD or L-MD group based on the GSEA (MSigDB V6.1), Related to Figure 2A-C (A-C) Normalized Enrichment scores (NES) for either H-MD or L-MD group were shown in colored scale according to the GSEA based on the gene-sets

of cancer hallmark (A), Reactome pathway (B), and cellular component (GO:CC) (C) from the MSigDB V6.1. NES are shown in colored scale, respectively.

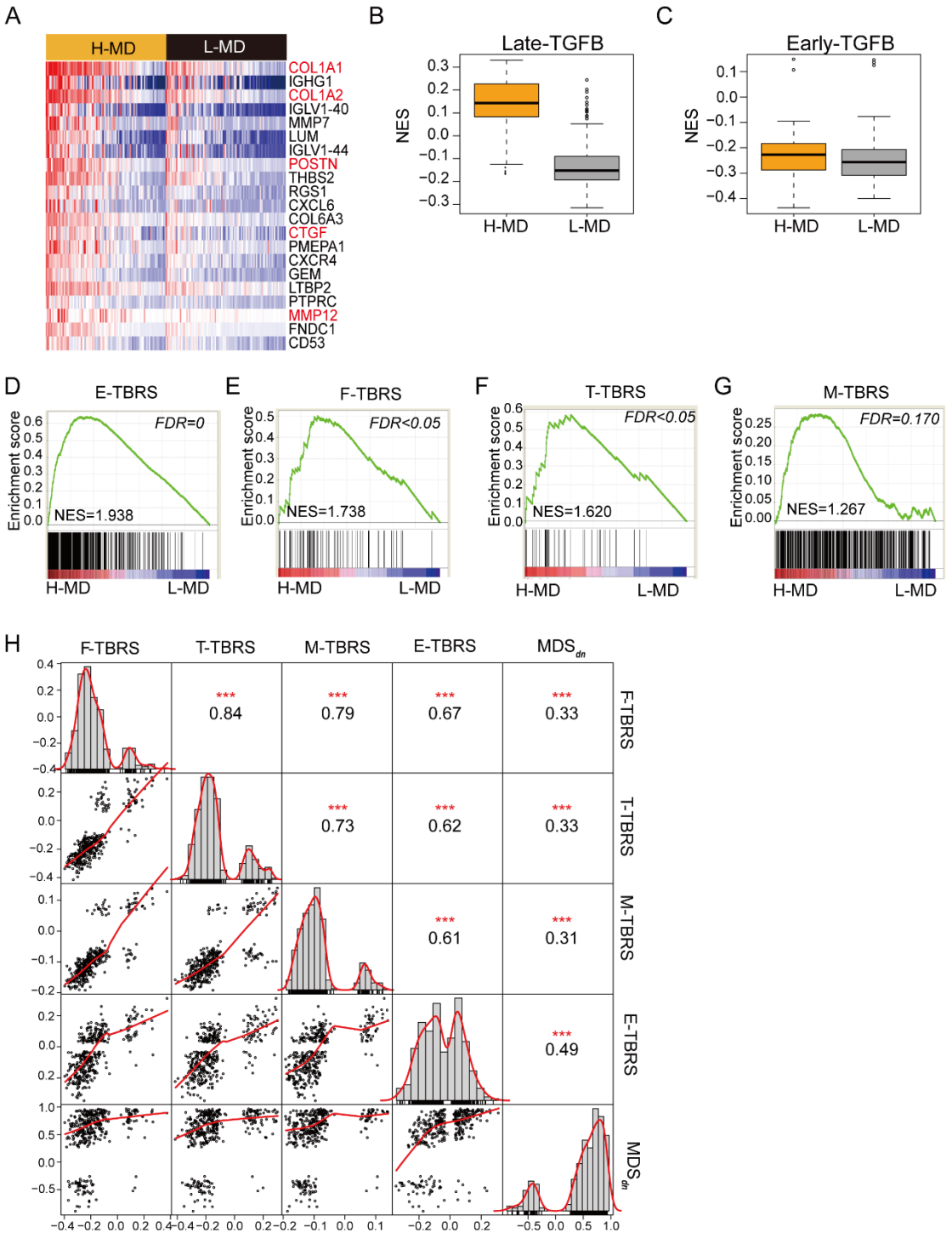

Figure S4. Association of mitoribosome defects with the microenvironment of HCC, Related to Figure 3C-D (A) Heatmap shows the expression of genes differentially expressed between H-MD and L-MD among the HCC immunity-related genes (ref. Figure 3A). Genes regarding the extracellular matrix are marked in red. (B-C) preRanked GSEA was performed based on the late (B) or early TGF-b response signatures (TBRS) (C). Boxplots of NES of samples from either H-MD or L-MD samples are shown as first quartile, median, and third quartile (bottom box, middle line, and top box, respectively) with Welch Two Sample t-test p value. Whiskers represent minimum and maximum values. (D-G) GSEA was performed based on the TBRS of Endothelial cells (E-TBRS) (D), Fibroblasts (F-TBRS)(E), T-Cells (T-TBRS)(F),

Macrophages (M-TBRS)(G) in H-MD versus L-MD samples. NES and FDR are depicted in each plot. (H) Cross-correlations among MDS_{dn}, F-TBRS, T-TBRS, M-TBRS, and E-TBRS in the patient cohort are shown. Correlation coefficients based on the Pearson's product-moment correlation are marked in each association ($^{***}p < 0.001$).

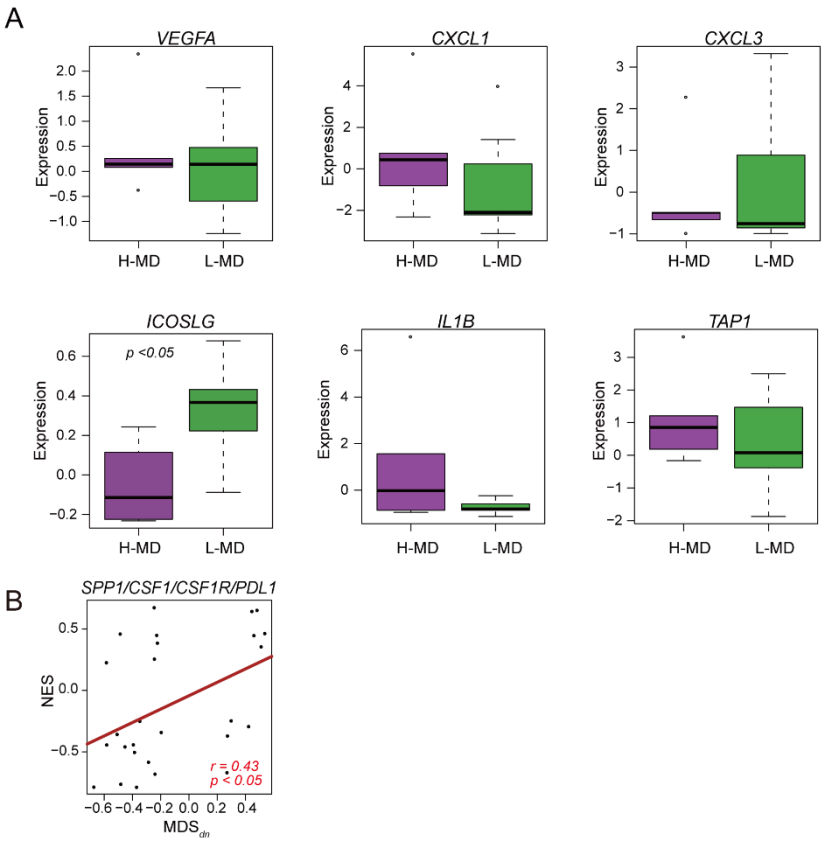

Figure S5. Validation of the mitoribosome defect associated cytokine in HCC cell line, Related to Figure 3G-I (A) Boxplots of mitoribosome defect-associated cytokines, which are differentially expressed between H-MD and L-MD group and have a significant association with MDS_{dn} in TCGA-HCC cohort (Related to Figure 3H), from H-MD and L-MD type HCC cell lines are shown as first quartile, median, and third quartile (bottom box, middle line, and top box, respectively). Only p-value with significance based on the Welch t-test between H-MD and L-MD type is depicted in the boxplot. (B) preRanked GSEA was performed based on the *SPP1/CSF1/CSF1R/PDL1*signal axis signature, which is related to a sensitivity of anti-PD-1 immunotherapy in HCC patients. The association *SPP1/CSF1/CSF1R/PDL1*signal axis with MDS_{dn} was examined. Correlation estimates and p-value are depicted in the plot. (C).

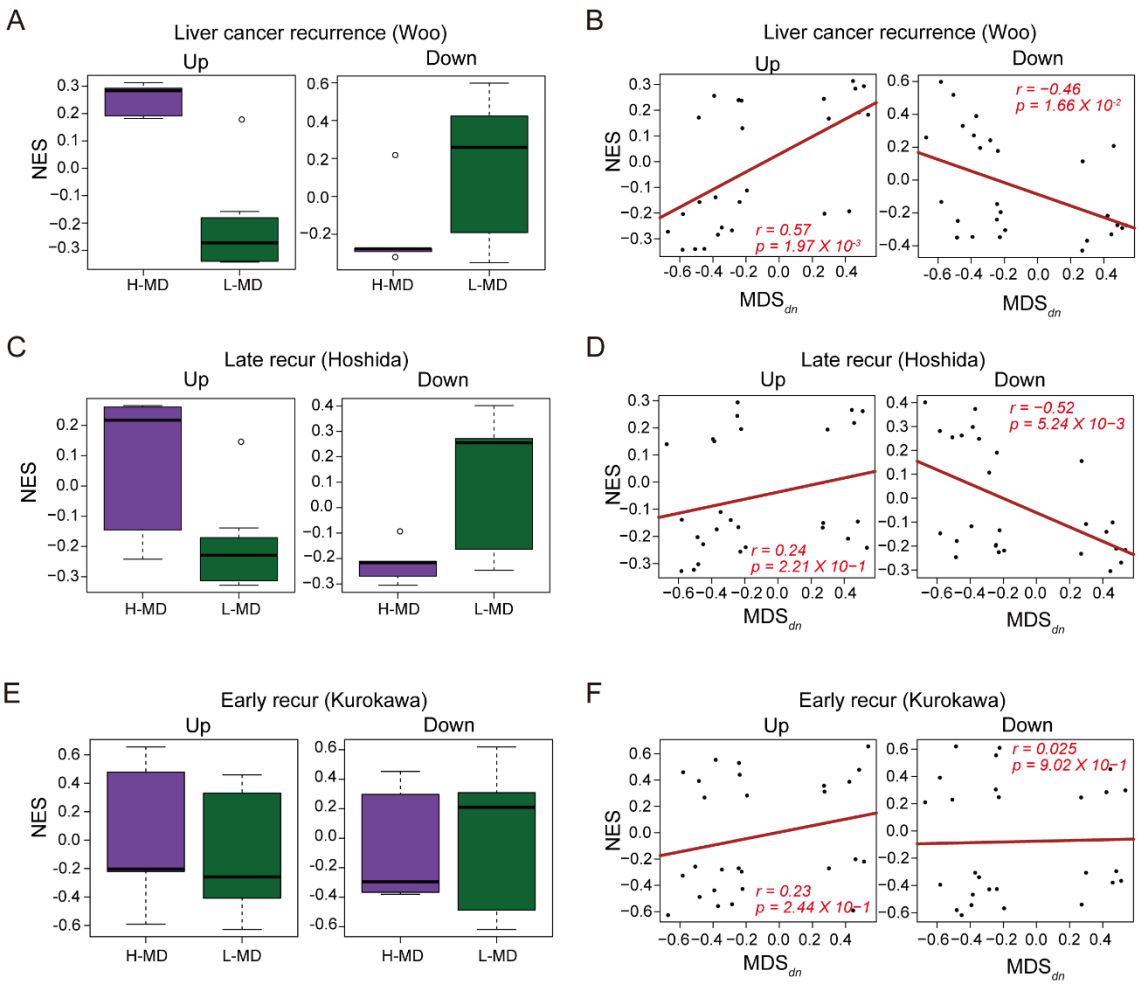

Figure S6. Association of MRP defect with HCC recurrence, Related to Figure 5D-E (A-F) preRanked GSEA was performed based on the several recurrence-related signatures, such as Liver cancer recurrence(A-B), late (C-D) or early recurrence-signatures (E-F). The enrichment for the up- (left) or down-regulated genes (right) related to each recurrence signature is compared between H-MD and L-MD type HCC cell lines (A, C, and E). The associations of MDS_{dn} with up- (left) or down-regulated genes (right) of each recurrence signature are shown in (B), (D), and (F). Correlation coefficients and p-values are depicted in each association. Boxplot of NES from H-MD and L-MD type HCC cell lines are as first quartile, median, and third quartile (bottom box, middle line, and top box, respectively) with Welch's two samples t-test p values. Whiskers represent the minimum and maximum values.

Supplemental Tables

Table S1. Sample information for 15 HCC patients from the Ajou Human Bio-Resource Bank (AHBB), Related to Figure 1

Tissue No.	Age	Sex	TNM staging
1	68	M	I
2	58	M	I
3	43	M	II
4	52	M	II
5	49	M	II
6	56	M	II
7	36	M	III
8	52	F	III
9	39	M	III
10	61	F	III
11	36	M	III
12	49	M	IV
13	46	M	IV
14	70	M	IV
15	56	M	IV

Table S2. Classification of MRPs based on the permutation t-test between PT and NT, Related to Figure 1E

Gene	perm.p	FDR	PT (mean)	NT (mean)	FC	MAD	Group
MRPL24	2.887E-15	4.734E-14	0.100	-0.726	0.826	0.713	Up-MRPs
MRPL15	1.468E-04	4.012E-04	0.045	-0.299	0.344	0.592	Up-MRPs
MRPS21	0.000E+00	0.000E+00	0.111	-0.799	0.911	0.697	Up-MRPs
MRPL14	1.747E-07	1.102E-06	0.053	-0.410	0.463	0.609	Up-MRPs
MRPL13	4.119E-07	2.412E-06	0.066	-0.442	0.507	0.670	Up-MRPs
MRPL21	1.783E-03	3.566E-03	0.037	-0.276	0.314	0.548	Up-MRPs
MRPS34	1.937E-06	9.929E-06	0.046	-0.350	0.396	0.583	Up-MRPs
MRPL47	7.623E-06	3.125E-05	0.044	-0.306	0.350	0.510	Up-MRPs
MRPS12	2.102E-09	1.723E-08	0.073	-0.521	0.594	0.611	Up-MRPs
MRPL9	1.132E-14	1.548E-13	0.075	-0.553	0.628	0.566	Up-MRPs
MRPL55	8.136E-08	6.065E-07	0.069	-0.506	0.575	0.747	Up-MRPs
MRPL52	1.781E-04	4.712E-04	0.042	-0.305	0.347	0.560	Up-MRPs
MRPL40	2.176E-01	2.664E-01	-0.013	0.087	-0.100	0.570	Other-MRPs
AURKAIP1	9.134E-01	9.134E-01	0.001	0.010	-0.010	0.621	Other-MRPs
MRPS28	2.645E-01	3.190E-01	-0.008	0.092	-0.100	0.596	Other-MRPs
MRPS15	8.914E-03	1.589E-02	0.024	-0.188	0.212	0.522	Other-MRPs
MRPL28	1.056E-02	1.842E-02	0.026	-0.191	0.218	0.543	Other-MRPs
MRPL36	4.767E-02	6.740E-02	0.017	-0.131	0.149	0.532	Other-MRPs
MRPS17	1.212E-02	2.029E-02	0.024	-0.171	0.195	0.527	Other-MRPs
MRPL18	3.044E-04	7.131E-04	0.035	-0.259	0.294	0.601	Other-MRPs
MRPL27	1.644E-02	2.696E-02	0.026	-0.188	0.214	0.571	Other-MRPs
MRPL20	4.012E-01	4.634E-01	-0.007	0.061	-0.068	0.548	Other-MRPs
MRPS33	5.218E-01	5.943E-01	0.005	-0.042	0.047	0.518	Other-MRPs
MRPL1	9.157E-04	1.976E-03	-0.028	0.224	-0.252	0.571	Other-MRPs
MRPL57	3.306E-02	5.021E-02	-0.024	0.148	-0.172	0.550	Other-MRPs
MRPL2	1.394E-01	1.874E-01	0.013	-0.102	0.115	0.549	Other-MRPs
MRPL23	3.571E-02	5.229E-02	0.026	-0.190	0.216	0.645	Other-MRPs
MRPS24	5.643E-01	6.339E-01	0.003	-0.044	0.048	0.512	Other-MRPs
MRPL41	6.498E-01	7.105E-01	-0.002	0.049	-0.051	0.751	Other-MRPs
MRPS18B	7.163E-03	1.305E-02	0.025	-0.205	0.230	0.574	Other-MRPs
MRPS26	6.027E-04	1.336E-03	0.031	-0.239	0.270	0.514	Other-MRPs
MRPL12	1.683E-01	2.156E-01	0.015	-0.125	0.140	0.676	Other-MRPs
MRPL39	8.235E-12	9.646E-11	-0.061	0.451	-0.512	0.509	Down-MRPs
MRPL46	1.869E-10	1.703E-09	-0.064	0.471	-0.535	0.582	Down-MRPs
MRPL34	2.675E-05	9.537E-05	-0.042	0.319	-0.361	0.548	Down-MRPs
MRPS6	1.076E-04	3.042E-04	-0.032	0.276	-0.308	0.552	Down-MRPs
MRPL54	9.730E-04	2.046E-03	-0.041	0.271	-0.312	0.571	Down-MRPs
MRPS31	1.380E-05	5.387E-05	-0.042	0.303	-0.346	0.607	Down-MRPs
MRPS11	1.953E-01	2.426E-01	0.008	-0.068	0.076	0.415	Unvariable
PTCD3	1.482E-01	1.961E-01	-0.013	0.067	-0.080	0.380	Unvariable
MRPL22	1.098E-02	1.876E-02	0.023	-0.156	0.179	0.471	Unvariable
MRPL10	2.194E-06	1.058E-05	0.031	-0.276	0.307	0.361	Unvariable

MRPS16	3.505E-05	1.197E-04	0.027	-0.210	0.237	0.355	Unvariable
DAP3	0.000E+00	0.000E+00	0.086	-0.622	0.708	0.496	Unvariable
MRPS27	1.728E-01	2.180E-01	0.010	-0.076	0.086	0.417	Unvariable
MRPS35	7.220E-01	7.790E-01	0.002	-0.022	0.024	0.391	Unvariable
MRPL38	1.944E-03	3.795E-03	0.012	-0.145	0.157	0.337	Unvariable
MRPS10	2.682E-04	6.467E-04	0.026	-0.205	0.231	0.404	Unvariable
MRPS9	8.076E-01	8.600E-01	0.006	-0.010	0.015	0.395	Unvariable
MRPS18A	6.893E-03	1.285E-02	0.024	-0.172	0.196	0.460	Unvariable
MRPL51	1.227E-07	8.386E-07	0.047	-0.346	0.393	0.496	Unvariable
MRPL53	0.000E+00	0.000E+00	0.063	-0.484	0.547	0.414	Unvariable
MRPL35	3.682E-01	4.313E-01	-0.004	0.045	-0.048	0.341	Unvariable
MRPS2	6.840E-05	2.157E-04	-0.036	0.282	-0.318	0.497	Unvariable
MRPL11	2.319E-02	3.729E-02	0.018	-0.146	0.164	0.429	Unvariable
MRPL58	5.340E-04	1.216E-03	0.022	-0.220	0.242	0.425	Unvariable
MRPL49	1.571E-01	2.045E-01	0.008	-0.086	0.094	0.426	Unvariable
MRPL30	6.460E-02	8.978E-02	0.011	-0.084	0.095	0.327	Unvariable
MRPS30	2.838E-02	4.391E-02	-0.013	0.105	-0.118	0.381	Unvariable
MRPL19	4.583E-06	1.978E-05	-0.029	0.238	-0.268	0.379	Unvariable
MRPS25	8.454E-01	8.775E-01	0.003	-0.012	0.015	0.484	Unvariable
MRPL44	2.158E-04	5.529E-04	-0.026	0.196	-0.222	0.361	Unvariable
MRPS22	1.191E-03	2.442E-03	-0.020	0.148	-0.167	0.316	Unvariable
MRPS5	6.434E-01	7.105E-01	0.007	-0.021	0.028	0.394	Unvariable
MRPS23	6.661E-16	1.366E-14	0.061	-0.510	0.571	0.410	Unvariable
CHCHD1	8.542E-05	2.502E-04	0.032	-0.259	0.292	0.497	Unvariable
MRPL37	3.392E-03	6.468E-03	-0.027	0.191	-0.217	0.472	Unvariable
MRPS14	2.506E-05	9.342E-05	0.032	-0.238	0.270	0.394	Unvariable
MRPS36	3.556E-02	5.229E-02	-0.021	0.140	-0.161	0.478	Unvariable
MRPS18C	2.616E-04	6.467E-04	-0.026	0.171	-0.198	0.386	Unvariable
MRPL4	8.216E-01	8.637E-01	-0.005	0.011	-0.017	0.489	Unvariable
MRPL45	7.489E-02	1.024E-01	0.013	-0.119	0.132	0.463	Unvariable
MRPL33	6.299E-07	3.444E-06	0.043	-0.351	0.394	0.469	Unvariable
MRPL42	3.043E-01	3.617E-01	0.004	-0.036	0.040	0.261	Unvariable
MRPL43	4.232E-02	6.088E-02	0.012	-0.114	0.126	0.388	Unvariable
MRPL50	8.706E-01	8.872E-01	-0.001	-0.013	0.012	0.485	Unvariable
MRPL32	2.131E-11	2.184E-10	-0.047	0.365	-0.412	0.408	Unvariable
MRPL16	5.475E-05	1.796E-04	-0.026	0.208	-0.234	0.347	Unvariable
MRPL3	8.764E-01	8.872E-01	0.002	-0.008	0.010	0.409	Unvariable
MRPS7	7.655E-05	2.325E-04	0.024	-0.234	0.258	0.434	Unvariable
MRPL17	4.265E-06	1.943E-05	0.047	-0.325	0.371	0.498	Unvariable
MRPL48	2.457E-02	3.874E-02	0.017	-0.122	0.139	0.412	Unvariable

Table S3. Association of Up-MRPs or Down-MRPs with Cancer Hallmark signature, Related to Figure 1F

Hallmark_Gene Set	Class	Up-MRPs		Down-MRP	
		cor.r	cor.p	cor.r	cor.p
TNFA_SIGNALING_VIA_NFKB	Common	-0.38772	9.338E-15	0.33536	3.340E-11
HYPOXIA	Common	-0.41043	1.653E-16	0.22364	1.372E-05
MITOTIC_SPINDLE	Common	-0.40772	2.721E-16	0.58103	7.051E-35
TGF_BETA_SIGNALING	Common	-0.48732	1.592E-23	0.36911	2.032E-13
IL6_JAK_STAT3_SIGNALING	Common	-0.33645	2.860E-11	0.33452	3.765E-11
DNA_REPAIR	Common	0.54719	2.312E-30	-0.28941	1.366E-08
APOPTOSIS	Common	-0.40976	1.870E-16	0.40192	7.780E-16
NOTCH_SIGNALING	Common	-0.29286	9.014E-09	0.2967	5.631E-09
ESTROGEN_RESPONSE_EARLY	Common	-0.50723	1.193E-25	0.32901	8.166E-11
ESTROGEN_RESPONSE_LATE	Common	-0.35429	2.058E-12	0.27203	1.022E-07
ANDROGEN_RESPONSE	Common	-0.56106	3.766E-32	0.26797	1.605E-07
MYOGENESIS	Common	-0.34416	9.358E-12	0.26484	2.259E-07
PROTEIN_SECRETION	Common	-0.40924	2.059E-16	0.42766	6.270E-18
INTERFERON_GAMMA_RESPONSE	Common	-0.20196	8.954E-05	0.23437	5.047E-06
APICAL_JUNCTION	Common	-0.41171	1.306E-16	0.47001	8.713E-22
APICAL_SURFACE	Common	-0.42077	2.375E-17	0.32628	1.192E-10
HEDGEHOG_SIGNALING	Common	-0.40461	4.785E-16	0.23646	4.132E-06
COMPLEMENT	Common	-0.35899	1.000E-12	0.28449	2.449E-08
PI3K_AKT_MTOR_SIGNALING	Common	-0.26113	3.368E-07	0.443	2.896E-19
MYC_TARGETS_V1	Common	0.21916	2.055E-05	0.19291	1.852E-04
EPITHELIAL_MESENCHYMAL_TRANSITION	Common	-0.38551	1.360E-14	0.32406	1.614E-10
INFLAMMATORY_RESPONSE	Common	-0.36885	2.119E-13	0.32066	2.561E-10
XENOBIOTIC_METABOLISM	Common	-0.19725	1.313E-04	-0.24183	2.448E-06
OXIDATIVE_PHOSPHORYLATION	Common	0.39933	1.234E-15	-0.56533	1.020E-32
P53_PATHWAY	Common	-0.28621	2.001E-08	0.2551	6.374E-07
UV_RESPONSE_DN	Common	-0.60956	4.073E-39	0.30286	2.614E-09
ANGIOGENESIS	Common	-0.37511	7.696E-14	0.32487	1.444E-10
HEME_METABOLISM	Common	-0.39883	1.348E-15	0.18676	2.981E-04
IL2_STAT5_SIGNALING	Common	-0.32492	1.436E-10	0.28008	4.092E-08
BILE_ACID_METABOLISM	Common	-0.17154	9.079E-04	-0.20518	6.859E-05
KRAS_SIGNALING_UP	Common	-0.37549	7.225E-14	0.2529	8.006E-07
CHOLESTEROL_HOMEOSTASIS	Down-Specific	-0.08968	8.454E-02	0.1809	4.627E-04
WNT_BETA_CATENIN_SIGNALING	Down-Specific	-0.13858	7.516E-03	0.25409	7.079E-07

G2M_CHECKPOINT	Down-Specific	0.00985	8.501E-01	0.39939	1.221E-15
ADIPOGENESIS	Down-Specific	-0.12792	1.367E-02	-0.28857	1.511E-08
INTERFERON_ALPHA_RESPONSE	Down-Specific	-0.13305	1.030E-02	0.20958	4.731E-05
UNFOLDED_PROTEIN_RESPONSE	Down-Specific	-0.15786	2.292E-03	0.41676	5.083E-17
MTORC1_SIGNALING	Down-Specific	-0.11934	2.149E-02	0.40226	7.313E-16
E2F_TARGETS	Down-Specific	0.09021	8.270E-02	0.30877	1.229E-09
FATTY_ACID_METABOLISM	Down-Specific	-0.11603	2.542E-02	-0.35561	1.683E-12
GLYCOLYSIS	Down-Specific	-0.13252	1.061E-02	0.30832	1.303E-09
UV_RESPONSE_UP	Down-Specific	-0.03408	5.129E-01	0.30503	1.985E-09
ALLOGRAFT_REJECTION	Down-Specific	-0.13325	1.019E-02	0.22264	1.503E-05
SPERMATOGENESIS	Down-Specific	0.16736	1.214E-03	0.23482	4.834E-06
MYC_TARGETS_V2	Up-Specific	0.52908	3.782E-28	-0.07169	1.682E-01
REACTIVE_OXIGEN_SPECIES_PATHWAY	Up-Specific	0.23808	3.533E-06	0.13448	9.506E-03
COAGULATION	Up-Specific	-0.42623	8.287E-18	-0.00402	9.385E-01
PEROXISOME	Up-Specific	-0.17123	9.283E-04	-0.11476	2.708E-02
KRAS_SIGNALING_DN	Up-Specific	-0.26817	1.569E-07	-0.05866	2.597E-01
PANCREAS_BETA_CELLS	Up-Specific	-0.26386	2.511E-07	-0.00215	9.671E-01

Table S6. Comparison of cells in the microenvironment of H-MD and L-MD subtype based on the xCell output, Related to Figure 3E-F

Cell	perm.p	FDR	H-MD (mean)	L-MD (mean)	Fold Change	Cell Type
Epithelial cells	6.765E-04	4.330E-03	0.1767	0.0994	0.0773	Others
Smooth muscle	1.286E-03	7.372E-03	0.2952	0.2546	0.0406	Stromal
CD4+ memory T-cells	5.328E-02	1.176E-01	0.1319	0.1063	0.0256	Leucocyte
B-cells	1.624E-01	2.665E-01	0.0465	0.0230	0.0235	Leucocyte
Mesangial cells	4.816E-07	1.027E-05	0.0212	0.0028	0.0184	Others
Fibroblasts	3.344E-03	1.338E-02	0.0332	0.0154	0.0178	Stromal
Sebocytes	2.109E-01	3.139E-01	0.0715	0.0588	0.0127	Others
Th2 cells	1.314E-02	4.426E-02	0.0243	0.0131	0.0112	Leucocyte
CD4+ naive T-cells	1.775E-01	2.840E-01	0.0212	0.0100	0.0112	Leucocyte
Mast cells	5.594E-04	4.330E-03	0.0187	0.0082	0.0105	Myeolid
aDC	6.433E-02	1.328E-01	0.0163	0.0060	0.0104	Myeolid
Tregs	2.038E-03	9.316E-03	0.0314	0.0218	0.0096	Leucocyte
Chondrocytes	3.489E-02	9.710E-02	0.0149	0.0061	0.0088	Stromal
Astrocytes	4.438E-03	1.671E-02	0.0111	0.0048	0.0062	Others
Class-switched memory B-cells	1.382E-03	7.372E-03	0.0089	0.0032	0.0057	Leucocyte
Keratinocytes	7.921E-02	1.536E-01	0.0106	0.0072	0.0034	Others
CD4+ T-cells	5.552E-02	1.184E-01	0.0034	0.0005	0.0029	Leucocyte
DC	4.477E-01	5.407E-01	0.0227	0.0200	0.0028	Myeolid
Memory B-cells	3.555E-01	4.644E-01	0.0036	0.0009	0.0027	Leucocyte
Myocytes	5.173E-02	1.176E-01	0.0123	0.0097	0.0026	Stromal
naive B-cells	2.409E-01	3.485E-01	0.0038	0.0013	0.0025	Leucocyte
Neutrophils	2.053E-01	3.129E-01	0.0017	0.0001	0.0016	Myeolid
iDC	7.770E-01	8.724E-01	0.0117	0.0104	0.0012	Myeolid
Pericytes	2.865E-01	3.987E-01	0.0012	0.0000	0.0012	Stromal
Melanocytes	2.135E-02	6.832E-02	0.0011	0.0003	0.0008	Others
Neurons	4.667E-02	1.106E-01	0.0011	0.0004	0.0007	Others
Eosinophils	3.857E-02	9.873E-02	0.0007	0.0001	0.0006	Myeolid
NK cells	3.787E-02	9.873E-02	0.0005	0.0000	0.0005	Leucocyte
CD8+ T-cells	9.594E-01	9.870E-01	0.0138	0.0135	0.0003	Leucocyte
Skeletal muscle	3.108E-01	4.144E-01	0.0000	0.0000	0.0000	Stromal
MPP	4.000E-01	5.120E-01	0.0000	0.0000	0.0000	Stem cell
Tgd cells	8.960E-01	9.557E-01	0.0000	0.0000	0.0000	Leucocyte
Platelets	8.381E-01	9.091E-01	0.0000	0.0000	0.0000	Stem cell
CD8+ Tcm	9.947E-01	9.947E-01	0.0133	0.0133	0.0000	Leucocyte
Basophils	9.716E-01	9.870E-01	0.0072	0.0073	-0.0002	Myeolid
Macrophages M1	9.498E-01	9.870E-01	0.0243	0.0246	-0.0003	Myeolid
CD4+ Tcm	6.825E-01	7.800E-01	0.0034	0.0037	-0.0004	Leucocyte
cDC	8.292E-01	9.091E-01	0.0078	0.0083	-0.0005	Myeolid
Preadipocytes	1.561E-01	2.628E-01	0.0000	0.0007	-0.0007	Stromal
CMP	1.918E-01	2.994E-01	0.0003	0.0013	-0.0010	Stem cell
Megakaryocytes	1.222E-01	2.172E-01	0.0020	0.0030	-0.0011	Stem cell
GMP	1.307E-01	2.260E-01	0.0005	0.0020	-0.0014	Stem cell

CD8+ Tem	5.394E-01	6.276E-01	0.0056	0.0073	-0.0017	Leucocyte
mv Endothelial cells	4.126E-01	5.178E-01	0.0041	0.0059	-0.0018	Stromal
CD4+ Tem	4.261E-01	5.244E-01	0.0184	0.0204	-0.0020	Leucocyte
pro B-cells	7.300E-02	1.460E-01	0.0038	0.0065	-0.0027	Leucocyte
Erythrocytes	3.003E-01	4.089E-01	0.0011	0.0038	-0.0027	Stem cell
Monocytes	5.331E-01	6.276E-01	0.0098	0.0125	-0.0028	Myeolid
CD8+ naive T-cells	3.121E-06	4.382E-05	0.0099	0.0148	-0.0049	Leucocyte
Macrophages M2	4.550E-02	1.106E-01	0.0168	0.0221	-0.0053	Myeolid
Plasma cells	1.513E-03	7.450E-03	0.0261	0.0332	-0.0071	Leucocyte
NKT	3.231E-02	9.399E-02	0.0368	0.0468	-0.0100	Leucocyte
MSC	1.165E-01	2.130E-01	0.0176	0.0285	-0.0109	Stromal
Macrophages	1.073E-01	2.019E-01	0.0597	0.0715	-0.0118	Myeolid
HSC	2.450E-01	3.485E-01	0.1120	0.1287	-0.0167	Stem cell
CLP	3.423E-06	4.382E-05	0.0365	0.0559	-0.0194	Stem cell
Endothelial cells	2.258E-02	6.881E-02	0.0758	0.1015	-0.0258	Stromal
Osteoblast	6.557E-06	6.994E-05	0.1423	0.1681	-0.0258	Stromal
pDC	5.527E-03	1.965E-02	0.1520	0.1870	-0.0350	Myeolid
MEP	1.277E-14	8.173E-13	0.0712	0.1068	-0.0356	Stem cell
Th1 cells	3.494E-08	1.118E-06	0.1053	0.1534	-0.0482	Leucocyte
Adipocytes	2.346E-03	1.001E-02	0.2376	0.3023	-0.0647	Stromal
ly Endothelial cells	6.565E-04	4.330E-03	0.0986	0.1702	-0.0716	Stromal
Hepatocytes	6.355E-05	5.810E-04	3.1131	3.7303	-0.6172	Others

Table S7. Permutation t-test between H-MD and L-MD subtype among immunomodulatory genes, Related to Figure 3G

Symbol	Class	Permutation t-test					Association w/ MRPs defects	
		perm. p	FDR	H-MD (mean)	L-MD (mean)	Fold change	Cor.R	Cor.p-value
TGFB1	Immunoinhibitor	0.000	0.000	0.467	-0.188	0.655	0.285	0.000
PDCD1	Immunoinhibitor	0.000	0.002	0.396	0.077	0.319	0.194	0.000
VEGFA	Immunoinhibitor	0.000	0.000	0.291	-0.117	0.409	0.394	0.000
CTLA4	Immunoinhibitor	0.022	0.049	0.267	0.145	0.122	0.142	0.006
IDO1	Immunoinhibitor	0.580	0.663	0.220	0.176	0.044	0.048	0.361
TNFRSF14	Immunoinhibitor	0.191	0.266	0.137	0.050	0.087	0.077	0.138
TGFBR1	Immunoinhibitor	0.006	0.024	0.111	-0.047	0.158	0.150	0.004
CXCL1	Immunoinhibitor	0.000	0.001	0.016	-0.681	0.697	0.309	0.000
CSF2	Immunoinhibitor	0.039	0.077	0.013	0.000	0.013	0.158	0.002
BTLA	Immunoinhibitor	0.460	0.552	-0.012	-0.025	0.014	0.073	0.162
CXCL3	Immunoinhibitor	0.000	0.001	-0.028	-0.196	0.168	0.266	0.000
CSF1	Immunoinhibitor	0.000	0.000	-0.055	-0.508	0.454	0.299	0.000
IL10RB	Immunoinhibitor	0.707	0.771	-0.110	-0.129	0.019	0.023	0.665
CSF3	Immunoinhibitor	0.084	0.136	-0.114	-0.105	-0.009	-0.121	0.020
CXCL8	Immunoinhibitor	0.000	0.000	-0.228	-0.962	0.734	0.329	0.000
IL10	Immunoinhibitor	0.115	0.173	-0.278	-0.310	0.032	0.055	0.292
CD160	Immunoinhibitor	0.011	0.033	-0.345	-0.304	-0.041	-0.125	0.016
TGFBR2	Immunoinhibitor	0.839	0.863	-0.362	-0.380	0.018	0.027	0.606
LAG3	Immunoinhibitor	0.815	0.850	-0.363	-0.384	0.021	0.015	0.777
CD274	Immunoinhibitor	0.765	0.813	-0.422	-0.410	-0.013	0.028	0.590
PTGER2	Immunoinhibitor	0.334	0.411	-0.436	-0.471	0.035	0.059	0.255
PDCD1LG2	Immunoinhibitor	0.205	0.279	-0.523	-0.585	0.062	0.049	0.350
PTGS2	Immunoinhibitor	0.060	0.106	-0.643	-0.698	0.055	0.156	0.003
CCL2	Immunoinhibitor	0.085	0.136	-1.225	-1.448	0.223	0.170	0.001
CXCL2	Immunoinhibitor	0.017	0.046	-2.081	-1.681	-0.400	-0.107	0.039
TNFRSF18	Immunostimulator	0.036	0.074	0.597	0.438	0.159	0.122	0.019
TNFSF4	Immunostimulator	0.066	0.111	0.464	0.351	0.113	0.096	0.065
TNFSF9	Immunostimulator	0.020	0.047	0.272	0.150	0.122	0.171	0.001
CD70	Immunostimulator	0.192	0.266	0.130	0.076	0.054	0.066	0.208
CD28	Immunostimulator	0.004	0.017	0.093	0.005	0.088	0.152	0.003
ICOS	Immunostimulator	0.011	0.033	0.087	0.005	0.082	0.170	0.001
IL12A	Immunostimulator	0.093	0.142	0.078	0.050	0.027	0.082	0.116
CD27	Immunostimulator	0.041	0.080	0.056	-0.133	0.189	0.119	0.021
IL6R	Immunostimulator	0.018	0.047	0.054	0.319	-0.264	-0.187	0.000
TNFSF18	Immunostimulator	0.121	0.178	0.013	-0.016	0.029	0.110	0.035
IL1A	Immunostimulator	0.022	0.049	0.006	-0.004	0.011	0.137	0.008
IL2	Immunostimulator	0.864	0.876	-0.004	-0.005	0.001	0.000	1.000
IL12B	Immunostimulator	0.539	0.637	-0.004	-0.007	0.003	0.044	0.401
TNFRSF13C	Immunostimulator	0.015	0.042	-0.006	-0.079	0.073	0.163	0.002

IFNG	Immunostimulator	0.627	0.705	-0.020	-0.037	0.018	0.073	0.159
CD80	Immunostimulator	0.001	0.008	-0.030	-0.091	0.061	0.176	0.001
TNFRSF13B	Immunostimulator	0.285	0.367	-0.040	-0.055	0.014	0.067	0.198
ICOSLG	Immunostimulator	0.000	0.000	-0.041	0.017	-0.059	-0.269	0.000
CD40LG	Immunostimulator	0.337	0.411	-0.068	-0.106	0.038	0.055	0.291
TNF	Immunostimulator	0.046	0.087	-0.158	-0.215	0.058	0.204	0.000
TNFRSF17	Immunostimulator	0.053	0.095	-0.176	-0.272	0.096	0.109	0.035
IL18	Immunostimulator	0.010	0.033	-0.183	-0.406	0.223	0.204	0.000
TNFSF13B	Immunostimulator	0.030	0.063	-0.233	-0.373	0.140	0.136	0.009
TMEM173	Immunostimulator	0.066	0.111	-0.238	-0.388	0.150	0.088	0.090
CD86	Immunostimulator	0.004	0.019	-0.362	-0.539	0.177	0.162	0.002
IL6	Immunostimulator	0.768	0.813	-0.472	-0.485	0.014	0.028	0.596
TNFSF13	Immunostimulator	0.087	0.136	-0.475	-0.565	0.090	0.126	0.015
IL1B	Immunostimulator	0.000	0.001	-0.588	-0.738	0.150	0.214	0.000
HLA-A	MHC class1	0.000	0.000	1.205	0.707	0.498	0.318	0.000
TAP1	MHC class1	0.000	0.000	0.940	0.456	0.483	0.346	0.000
HLA-C	MHC class1	0.003	0.016	0.816	0.487	0.329	0.231	0.000
HLA-B	MHC class1	0.007	0.025	0.774	0.395	0.379	0.229	0.000
TAP2	MHC class1	0.918	0.918	0.440	0.447	-0.007	0.017	0.750
B2M	MHC class1	0.018	0.047	0.289	0.057	0.232	0.165	0.001
HLA-DRB1	MHC class2	0.050	0.092	0.061	-0.243	0.305	0.127	0.014
HLA-DQB2	MHC class2	0.002	0.010	0.006	-0.344	0.350	0.209	0.000
HLA-DPB2	MHC class2	0.694	0.769	-0.053	-0.074	0.021	0.025	0.632
HLA-DQB1	MHC class2	0.261	0.348	-0.053	-0.209	0.156	0.052	0.316
HLA-DRB5	MHC class2	0.281	0.367	-0.133	-0.315	0.182	0.049	0.351
HLA-DPB1	MHC class2	0.010	0.033	-0.158	-0.502	0.345	0.151	0.003
HLA-DQA2	MHC class2	0.010	0.033	-0.285	-0.678	0.393	0.146	0.005
HLA-DQA1	MHC class2	0.019	0.047	-0.335	-0.619	0.285	0.163	0.002
HLA-DPA1	MHC class2	0.020	0.047	-0.387	-0.716	0.329	0.118	0.024
HLA-DRB6	MHC class2	0.138	0.198	-0.431	-0.640	0.209	0.064	0.218
HLA-F	MHC non-class	0.563	0.653	0.551	0.479	0.072	0.050	0.339
HLA-E	MHC non-class	0.001	0.003	0.403	0.123	0.280	0.223	0.000
HLA-G	MHC non-class	0.308	0.390	0.215	0.300	-0.085	-0.061	0.237

Table S8. Classification of HCC cell line into H-MD and L-MD subtype based on the MRP defects score (MDS), Related to Figure 4A

Cell line	MDS	Class
NCIH684	-0.671	L-MD
HEPG2	-0.583	L-MD
PLCPRF5	-0.580	L-MD
C3A	-0.507	L-MD
SNU423	-0.485	L-MD
SNU398	-0.481	L-MD
JHH5	-0.451	L-MD
SNU182	-0.392	NA
HUH7	-0.384	NA
JHH7	-0.369	NA
HUH1	-0.346	NA
HUH6	-0.285	NA
SNU886	-0.245	NA
SNU761	-0.243	NA
HEP3B217	-0.239	NA
HLF	-0.227	NA
LI7	-0.222	NA
HLE	-0.194	NA
SKHEP1	0.270	NA
ALEXANDERCELLS	0.274	NA
JHH6	0.300	NA
JHH1	0.423	NA
SNU475	0.446	H-MD
SNU878	0.461	H-MD
JHH4	0.482	H-MD
JHH2	0.512	H-MD
SNU449	0.537	H-MD

Table S9. Association of MRP defects scores (MDS) in HCC cell line with liver cancer recurrence signature (MsigDB v6.1), Related to Figure 5D-E

GeneSet (MsigDB v6.1)	Association with MRP defect		t.test p.value (H-MD vs L-MD)
	cor.r	cor.p	p-value
IIZUKA_LIVER_CANCER_EARLY_RECURRENCE	0.063	7.55×10^{-1}	7.99×10^{-1}
HOSHIDA_LIVER_CANCER_LATE_RECURRENCE_UP	0.244	2.21×10^{-1}	7.27×10^{-2}
HOSHIDA_LIVER_CANCER_LATE_RECURRENCE_DN	-0.522	5.24×10^{-3}	2.21×10^{-2}
WOO_LIVER_CANCER_RECURRENCE_UP	0.569	1.97×10^{-3}	2.93×10^{-4}
WOO_LIVER_CANCER_RECURRENCE_DN	-0.457	1.66×10^{-2}	8.85×10^{-2}
YOSHIOKA_LIVER_CANCER_EARLY_RECURRENCE_UP	-0.164	4.12×10^{-1}	6.91×10^{-1}
YOSHIOKA_LIVER_CANCER_EARLY_RECURRENCE_DN	-0.256	1.97×10^{-1}	4.89×10^{-1}
KUROKAWA_LIVER_CANCER_EARLY_RECURRENCE_UP	0.232	2.44×10^{-1}	7.20×10^{-1}
KUROKAWA_LIVER_CANCER_EARLY_RECURRENCE_DN	0.025	9.02×10^{-1}	8.89×10^{-1}

Transparent Methods

Patients and tissue specimens

The paired tumor and the adjacent non-tumoral tissue samples from 15 HCC patients were obtained from the Ajou Human Bio-Resource Bank (AHBB), a member of the National Biobank of Korea, which is supported by the Ministry of Health and Welfare. Freshly frozen specimens from 15 cases of HCC tissues and 15 adjacent non-tumoral tissues were used for this study.

Data and Preprocessing

For HCC patient cohort, we obtained RNAseq data for TCGA liver cancer cohorts consisting of 371 primary tumors (PT) and 50 non-tumor tissues (NT) (https://docs.gdc.cancer.gov). We used FPKM values for each annotated gene symbol and processed to normalize each value based on the mean of each feature among NT. For validation in the HCC cell line, we used the RNAseq gene expression data from CCLE (Cancer Cell Line Encyclopedia) and used RPKM values to preprocess the expression value of each gene symbol. Transcriptome data for a total of 28 HCC cell line was used in further analysis.

Profiling of Mitoribosomal protein transcriptome

We performed a transcriptome profiling of 82 MRPs. First, to select variable MRPs among 82 MRPs, we applied the cut-off of MAD (> 0.5) and used them for further analysis. To identify the MRP defect associated signature comparing with expression among NT, we carried out permutation t-test between PT and NT and assigned selected MRPs into three categories, Up-MRPs, Dn-MPRs, and Other-MRPs, according to the FDR and fold change (FC) (FDR < 0.05 & FC > 0.3, FC < -0.3, or -0.3 < FC < 0.3, respectively).

Gene-set enrichment analysis (GSEA) and preRankedGSEA

To assess the enrichment of gene-sets of interest, we performed GSEA analysis and preRanked GSEA. GSEA was implemented using the software (**http://software.broadinstitute.org/gsea/downloads.jsp**)(Subramanian et al., 2005) based on the Molecular Signatures Database (MSigDB database v6.2). To calculate the normalized enrichment (NES) in the individual sample, we used preRanked GSEA method implemented in R package.

Calculation of MRP defect score (MDS)

Using the three defined MRP signatures (Up-MRPs, Dn-MRPs, and Other-MRPs), we calculated the NES by implementing preRanked GSEA. As the notion that aberrant expression of three MRP signatures was closely associated with the mitoribosome defect, we estimated MDS for Up-MRPs and Other-MRPs using NES. Since Dn-MRPs was depleted in PT compared to NT, we converted the pre-calculated NES for Dn-MRPs by multiplying -1 to reflect the direction and assigned this value into MDS_{dn} for each sample.

Classification of high (H) and low (L) MDS subtype

Using the MDS_{dn}, we stratified HCC samples into the one with high and low mitoribosome defect (MD) subtype, H-MD and L-MD, respectively, according to the upper or lower quartile of MDS_{dn} of overall samples, respectively.

Differentially Expressed Genes (DEG) and Gene Ontology (GO) analysis

By comparing the expression between H-MD and L-MD, we selected DEG in each subtype based on the fold change and permutation p-value from the permutation t-test with 1,000 re-sampling (FC > 1 or -1 & FDR <0.001). GO enrichment analysis was performed based on the DAVID 6.7(Huang da et al., 2009)

Estimation of mtDNA copy number

To estimate mtDNA copy number, two primer sets, a set for MT-ND2 gene for mitochondrial DNA and a set of 28S rRNA gene for nuclear DNA, were used to PCR analysis with the isolated total genomic DNA as a template. The sequences of the primer-sets used in this study were as follows: for MT-ND2, 5'-AGGTTACCCAAGGCACCCCT-3' and 5'-AGTAGATTAGGCGTAGGTAG-3'; for 28S rRNA, 5'-TAGCAGCCGACTTAGAACTGG-3' and 5'-CTCCCACTTATTCTACACCTC-3'. MtDNA copy number indicated as a ratio MT-DN2 level to 28S rRNA level.

Cell culture and cell growth rate

HepG2 and SNU475 cells were purchased from American Tissue Culture Collections (ATCC, Rockville, MD) and Korean Cell Line Bank (Seoul, Korea), respectively, and were cultured in Dulbecco's modified Eagle's medium (DMEM) (Invitrogen, Carlsbad, CA) and RPMI1640 medium (Invitrogen), respectively, supplemented with 10% fetal bovine serum (FBS) (Invitrogen) and antibiotics (Invitrogen) at 37°C in a humidified incubator with 5% CO_2. JHH4 and JHH5 cells were purchased from Japanese Collection of Research Bioresources Cell Bank (JCRB, Japan, Tokyo) and were cultured in Minimum Essential Media (MEM, Invitrogen) and William's Media E (Invitrogen), respectively, supplemented with 10% FBS (Invitrogen) and antibiotics (Invitrogen). Cell growth rates were monitored by the trypan blue-negative viable cells. After stabilization of cells for 48hr, cells were harvested by trypsinization and counted using the Countess™ automated cell counter (Invitrogen).

Sucrose gradient sedimentation analysis

The sedimentation properties of mitoribosomal proteins from whole-cell lysates were analyzed by sucrose gradient sedimentation as previously described (Kim and Barrientos, 2018) with slight modification. Whole cells were solubilized in 500μl lysis buffer [20mM HEPES, pH 7.4, 100 mM KCl, 20 mM $MgCl_2$, 0.5% Triton X-100, 1 mM Na_3VO_4, 1 mM NaF, 1 mM PMSF, 1.5 μg/ml pepstatin A, 1.5 μg/ml leupeptin, 40U/ml recombinant RNase inhibitor (Promega, Madison, WI)]. Whole-cell lysate (200 μg) was loaded onto a 2.75 ml linear 10% to 30% sucrose gradient containing 20mM HEPES (pH7.4), 100 mM KCl, 10 mM $MgCl_2$, 0.5% Triton X-100 and centrifugated at 40,000rpm for 3h 10m at 4°C using TLA-110 rotor and Beckman Optima™ MAX-XP Ultracentrifuge (Beckman Coulter, Brea, CA). After centrifugation, the gradients were collected from the bottom into 12 equal fractions and subjected to Western blot analysis.

Cell invasion assay

Cells (2 x 10^4) pre-starved with serum-free media for over-night were placed into the upper chamber with 100 µl of serum-free medium. Medium supplemented with 10% FBS was placed in the lower chamber as a chemo-attractant. The upper chamber, Transwell™ insert membranes (8-µm pore size, Corning, Acton, MA), was pre-coated with 7% Growth Factor Reduced BD Matrigel™ Matrix (Becton Dickinson Labware, Franklin Lakes, NJ) for the cell invasion assay. After 48hrs, the cells that invaded the lower surface were fixed with 100% methanol for 1 min, stained with Hematoxylin Solution (Sigma-Aldrich, Saint Louis, MI) and Eosin Y Solution (Sigma-Aldrich), and counted.

Western blot analysis

Western blotting was performed using standard procedures. Antibodies against mS31/MRPS31 (ab167406), uL13/MRPL13 (ab190232), uS15/MRPS15 (ab137070), SDHA (ab14715), and MT-COX2 (ab110258) were purchased from Abcam (Cambridge, MA). Antibodies against Smad2 (07-408) and p-Smad2 (05-953) were purchased from Upstate Biotechnology, Inc. (Lake Placid, NY). Ubiquitin (sc-8017) and actin (sc-47778) antibodies were obtained from Santa Cruz Biotech. (Dallas, TX) and VDAC (PC548) and α-tubulin (05-829) antibodies were from Millipore (Billerica, MA). Antibodies against mL46/MRPL46 (GTX87311), uS22/MRPS22 (GTX106558), and MT-ND6 (A31857) and were obtained from GeneTex Inc. (Irvine, CA), Invitrogen, and Proteintech (Rosemont, IL), respectively. Antibody for uL11/MRPL11(#2199S) was purchased from CST (Danvers, MA). Antibody for TFAM was kindly provided by Youngmi Kim Pak from Kyung Hee University (Seoul, South Korea).

Quantitative real-time RT-PCR (qPCR)

Total RNA was isolated using NucleoSpin® RNA Plus, kit (MACHEREY-NAGEL GmbH & Co. KG, Düren, Germany) and cDNA was synthesized using avian myeloblastosis virus (AMV) reverse transcriptase (Promega, Madison, WI). PCR was performed using THUNDERBIRD™ SYBR™ qPCR Mix (Toyobo Co., Ltd, Osaka, Japan) following the manufacturer's protocol. The PCR primer sets were produced by Bioneer (Daejeon, Korea) for TGF-β (5'-GCGTGCTAATGGTGGAAAC and 5'-CTGAGGTATCGCCAGGAA), CSF1 (5'-TCTCTGCAGCGGCTGATTG and 5'-TCTCTGAAGCGCATGGTGTC), β-actin (5'-CCTTCCTGGGCATGGAGTCCTGT and 5'-GGAGCAATGATCTTGATCTTC) and α-tubulin (5'-GGGCATGGACGAGATGGA and 5'-GGACACCAGGTCGTTCATGTT). Expression levels of target mRNAs were normalized by β-actin or α-tubulin mRNA levels.

Statistical Analyses

Kaplan-Meier (KM) Survival Analysis was performed based on the survival R package and p-value from the log-rank test based on the Cox Proportional-Hazards Regression model was used to compare overall survival. Permutation t-test was calculated based on the perm R package by 1,000 resamplings. Correlation coefficient and the p-value were calculated based on the Pearson's product-moment correlation.

Supplemental References

Huang da, W., Sherman, B. T. & Lempicki, R. A. 2009. Systematic and integrative analysis of large gene lists using DAVID bioinformatics resources. *Nat Protoc,* 4(1)**,** pp 44-57.

Kim, H. J. & Barrientos, A. 2018. MTG1 couples mitoribosome large subunit assembly with intersubunit bridge formation. *Nucleic Acids Res,* 46(16)**,** pp 8435-8453.

Subramanian, A., Tamayo, P., Mootha, V. K., Mukherjee, S., Ebert, B. L., Gillette, M. A., Paulovich, A., Pomeroy, S. L., Golub, T. R., Lander, E. S. & Mesirov, J. P. 2005. Gene set enrichment analysis: a knowledge-based approach for interpreting genome-wide expression profiles. *Proc Natl Acad Sci U S A,* 102(43)**,** pp 15545-50.